

Perceptual Error Optimization for Monte Carlo Rendering

VASSILLEN CHIZHOV, MIA Group Saarland University, Max-Planck-Institut für Informatik, Germany

ILIJAN GEORGIEV, Autodesk, United Kingdom

KAROL MYSZKOWSKI, Max-Planck-Institut für Informatik, Germany

GURPRIT SINGH, Max-Planck-Institut für Informatik, Germany



Fig. 1. Using our perception-motivated model, we analyze different ways to distribute screen-space error in Monte Carlo rendering, showing one such approach here. We start with a noisy image and some auxiliary data (surface normals and albedo). Average image (leftmost) is rendered with 16 samples per pixel (spp). Our method uses varying spp from the set: $\{4, 8, 12, 16\}$ spp. (a) Our approach exhibits both visually pleasing screen-space error distribution (see Section 4.1 for details) while keeping less samples per pixel. Our energy model uses a guiding image, or *surrogate*, which can be created easily from the noisy estimate. We also show our method using the ground truth (GT) image as the guide. (b) To demonstrate the impact of error distribution on denoising, we apply Intel’s Open Image Denoiser [int 2018] on the images in (a): the white-noise distribution results in conspicuous artifacts, which are avoided when the error has a blue-noise distribution (as in our results). (c) The corresponding tiled power spectrum (32×32 pixels per tile) of the *error* images from (a), confirming that our approach distributes error with a locally blue-noise spectrum.

Realistic image synthesis involves computing high-dimensional light transport integrals which in practice are numerically estimated using Monte Carlo integration. The error of this estimation manifests itself in the image as visually displeasing aliasing or noise. To ameliorate this, we develop a theoretical framework for optimizing screen-space error distribution. Our model is flexible and works for arbitrary target error power spectra. We focus on perceptual error optimization by leveraging models of the human visual system’s (HVS) point spread function (PSF) from halftoning literature. This results in a specific optimization problem whose solution distributes the error as visually pleasing blue noise in image space. We develop a set of algorithms that provide a trade-off between quality and speed, showing substantial improvements over prior state of the art. We perform evaluations using both quantitative and perceptual error metrics to support our analysis, and provide extensive supplemental material to help evaluate the perceptual improvements achieved by our methods.

Additional Key Words and Phrases: Monte Carlo, rendering, sampling, perceptual error, blue noise

Authors’ addresses: Vassillen Chizhov, MIA Group Saarland University, Max-Planck-Institut für Informatik, Saarbrücken, Germany; Iliyan Georgiev, Autodesk, United Kingdom; Karol Myszkowski, Max-Planck-Institut für Informatik, Saarbrücken, Germany; Gurprit Singh, Max-Planck-Institut für Informatik, Saarbrücken, Germany.

1 INTRODUCTION

Using (quasi) Monte Carlo (MC) sampling for rendering produces approximation error. This error can result in visually displeasing artifacts in the image, unless care is taken to control the correlation of the samples used to obtain the individual pixel estimates. A standard approach is to decorrelate these estimates by randomly assigning sample sets to pixels, turning potential structured artifacts into white noise.

In digital halftoning, the error induced by quantizing continuous tone images has been studied extensively. These studies have shown that a blue-noise distribution of the quantization error is perceptually optimal [Ulichney 1987] and can achieve substantially higher fidelity than a white-noise distribution. Recent works have proposed ways to transfer these ideas empirically to image synthesis [Georgiev and Fajardo 2016; Heitz and Belcour 2019; Heitz et al. 2019]. This is achieved by carefully re-introducing *negative* pixel correlation, exploiting the local smoothness present in typical images.

We propose a theoretical formulation of perceptual error for rendering which unifies previous methods in a common theoretical framework and justifies the need for blue-noise error distribution. We start by extending the comparatively simpler problem of digital

halftoning [Sullivan et al. 1991; Analoui and Allebach 1992; Pappas and Neuhoff 1999] to the substantially more complex one of MC image synthesis. Our formulation bridges the gap between halftoning and rendering by interpreting the error distribution problem as a general extension of non-uniform multitone energy minimization halftoning, where the MC estimates are taken to be the admissible quantization levels in the halftoning setting. Through this insight virtually any halftoning method can be adapted to work with MC rendering. We demonstrate this by adapting representative methods from the three main classes of halftoning algorithms: dither matrix halftoning, error diffusion halftoning, iterative energy minimization halftoning.

Previous methods [Georgiev and Fajardo 2016; Heitz and Belcour 2019; Heitz et al. 2019] work by distributing MC error via target error masks which are produced by minimizing an energy involving a pre-chosen kernel. The kernel, typically a Gaussian, can be interpreted as an approximation to the human visual system’s (HVS) point spread function (PSF) [Daly 1987; Pappas and Neuhoff 1999]. We revisit the kernel-based perceptual model from halftoning [Sullivan et al. 1991; Analoui and Allebach 1992; Pappas and Neuhoff 1999] and reformulate it for MC rendering. The resulting energy can be optimized for MC error distribution without any explicit mask. By providing a formal analysis, we make the hidden assumptions of previous methods explicit and quantify their limitations. Notably, all previous methods can be seen as variants of dither matrix halftoning introducing varying degrees of bias. In summary:

- Our formulation unifies both a-priori and a-posteriori methods. This removes the necessity of using empirically motivated energies, making all assumptions explicit, and prescribing general guidelines for devising new a-priori and a-posteriori methods in a principled manner.
- All a-posteriori methods in our framework can be seen as methods, which can be used to decrease the bias of a rendered biased image. This provides a continuous spectrum between the fully unbiased estimates (white noise error distribution) and highly biased such (high quality blue noise distribution). This insight makes the limitations of a-posteriori methods quantifiable.
- We demonstrate our theoretical results through several experiments that showcase that we can substantially improve the error distribution in rendering compared to all previous state of the art methods (Section 7) which aim to redistribute the error as blue noise. Notably, this is achieved while using the exact same rendering data as previous methods. These results include but are not limited to: suppressing fireflies, removing visually objectionable hallucinated artifacts from a denoiser, producing images closer to the ground truth after convolution, achieving a high quality blue noise error distribution in animations even in the presence of large temporal discontinuities.

Following an overview of relevant prior work (Section 2), we present necessary background and motivation in Section 3.1. We then devise our perceptual error formulation for image synthesis (Section 3.2) and present our algorithms for solving the proposed optimization problem (Section 4). We discuss extensions to our base model in Section 6, and demonstrate the benefits on several realistic scenes

in Section 7. We conclude with an outline of promising directions for future research (Section 8).

2 RELATED WORK

Our work draws from diverse research in imaging, rendering, and perception. We begin our exposition with a structured survey of relevant prior work in these fields.

2.1 Digital halftoning

Digital halftoning [Stoffel and Moreland 1981] involves creating the illusion of continuous-tone images through the arrangement of binary elements; various algorithms target different display devices. Bayer [1973] developed the widely used dispersed-dot ordered dither patterns. Allebach and Liu [1976] introduced the use of randomness in clustered-dot ordered dithering. Ulichney [1987] introduced *blue-noise* patterns that yield better perceptual quality. Mitsa and Parker [1991] mimic those patterns to produce ordered dither arrays for given spatial frequency domain characteristics. In 1993, Ulichney proposed the void-and-cluster algorithm which uses a Gaussian kernel to create dither masks with isotropic blue-noise distribution. Sullivan et al. [1991] capitalized on this kernel-based approach and developed an energy function in the Fourier domain to obtain visually optimal halftone patterns. Analoui and Allebach [1992] designed a spatial-domain interpretation of Sullivan et al.’s model, in order to develop a practical algorithm for blue-noise dithering. Their approach was later refined by Pappas and Neuhoff [1999].

Motivated by Ulichney’s [1993] approach, various structure-aware halftoning algorithms were developed in graphics [Ostromoukhov 2001; Pang et al. 2008; Chang et al. 2009]. In this work, we leverage the kernel-based model [Analoui and Allebach 1992; Pappas and Neuhoff 1999] in the context of Monte Carlo rendering [Kajiya 1986].

2.2 Quantitative error assessment in rendering

In rendering, the light transport integral estimation error (\mathcal{L}_1 , MSE, or RMSE) is usually reported as a single value evaluated over the whole image or a set of images. Since these metrics often do not accurately reflect the visual quality, equal-time visual comparisons are also commonly reported. Various theoretical frameworks have been developed in the spatial [Niederreiter 1992; Kuipers and Niederreiter 1974] and Fourier [Singh et al. 2019] domains to understand the error reported through these metrics. Numerous variance reduction algorithms like multiple importance sampling [Veach 1998], and control variates [Loh 1995; Glasserman 2004] improve the error convergence of light transport renderings. Recently, Celarek et al. [2019] proposed error spectrum ensemble (ESE), a tool for measuring the distribution of error over frequencies. ESE reveals correlation between pixels and can be used to detect outliers, which offset the amount of error substantially.

Many denoising methods [Zwicker et al. 2015] employ these metrics to optimize over noisy images to get noise-free renderings. Even if the most advanced denoising techniques driven by such metrics can efficiently steer adaptive sampling [Chaitanya et al. 2017; Kuznetsov et al. 2018; Kaplanyan et al. 2019], they emphasize

on the local sample density, and are incapable of indicating the optimal sample layout in screen space.

Contrary to aforementioned metrics, we develop a perceptual model for rendered images that focuses on the perceptually optimal distribution of error, i. e., with respect to the human visual system’s (HVS) modulation transfer function (MTF) [Daly 1987; Sullivan et al. 1991]. Our theoretical framework argues that the screen-space sample layout is crucial for perceptual fidelity, which the most commonly used error metrics do not capture.

2.3 Perceptual error assessment in rendering

Although substantial progress in the study of HVS is continuously made, well understood are mostly the early stages of the visual pathways from the eye optics, through the retina to the visual cortex. This limits the scope of existing computational models of the HVS that are used in imaging and computer graphics. Such models should additionally be computationally efficient and generalize over simplistic stimuli that have been used in their derivation through psychophysical experiments.

Contrast sensitivity function. The contrast sensitivity function (CSF) is one of the core HVS models that fulfills those conditions and comprehensively characterizes overall optical [Westheimer 1986; Deeley et al. 1991] and neural processes [Souza et al. 2011] in detecting contrast visibility as a function of spatial frequency. While originally it is modeled as a band-pass filter [Barten 1999; Daly 1993], its shape changes towards a low-pass filter with retinal eccentricity [Robson and Graham 1981; Peli et al. 1991] and reduced luminance adaptation in scotopic and mesopic levels [Wuerger et al. 2020]. Low-pass characteristics are also inherent for chromatic CSFs [Mullen 1985; Wuerger et al. 2020; Bolin and Meyer 1998]. In many practical imaging applications, e.g., JPEG compression [Rashid et al. 2005], rendering [Ramasubramanian et al. 1999], or halftoning [Pappas and Neuhoff 1999], the CSF is modeled as a low-pass filter, which also allows for a better control of image intensity. By normalizing such a CSF by the maximum contrast sensitivity value, a unitless function akin to the MTF can be derived [Daly 1987; Mannos and Sakrison 1974; Mantiuk et al. 2005; Sullivan et al. 1991; Souza et al. 2011] that after transforming from frequency to spatial domain results in the Point Spread Function (PSF) [Analoui and Allebach 1992; Pappas and Neuhoff 1999]. Following Pappas and Neuhoff [1999] we approximate such a PSF by a suitable Gaussian filter, where the error of such approximation becomes practically negligible for sample density of 300 dpi and the viewer distance to the screen beyond 60 cm.

Advanced quality metrics. More costly, and often less robust, modeling of the HVS beyond the CSF is performed at advanced quality metrics [Lubin 1995; Daly 1993; Mantiuk et al. 2011] that have been adapted to rendering where they guide the computation to the image regions where the visual error is most perceived [Bolin and Meyer 1995, 1998; Ramasubramanian et al. 1999; Ferwerda et al. 1996; Myszkowski 1998; Volevich et al. 2000]. An important application is visible noise reduction in ray and path tracing by content

Table 1. List of commonly used notations throughout the paper.

Symbol	Meaning
$\langle \cdot, \cdot \rangle, \odot, *$	inner product, element-wise product, convolution
$\ \cdot\ _2$	2-norm
$\mathbf{g}, \hat{\mathbf{g}}, \hat{\mathbf{g}} ^2$	convolution kernel, its Fourier and power spectra
$I, Q, \epsilon = Q - I$	reference image, estimated image, error image
S_i, \mathbf{S}	sample set for pixel i , sample sets for all pixels

adaptive sample density control [Bolin and Meyer 1995, 1998; Ramasubramanian et al. 1999]. Our framework enables further significant reduction of the noise visibility for the same sample budget.

Sampling in rendering. Sample correlations [Singh et al. 2019] directly affect the error in rendering. Quasi-Monte Carlo samplers [Halton 1964; Sobol 1967] preserve correlations (i. e., stratification) well in higher dimensions, which makes them a perfect candidate for rendering problems [Keller 2013]. However, imposing perceptual control over these samplers is not well studied. On the other hand, stochastic samplers are shown to have direct resemblance to the cone layout in the human eye [Yellott 1983]. This has inspired the development of various stochastic sample correlations in rendering [Cook 1986; Dippé and Wold 1985; Mitchell 1991], e. g., blue noise. In this work, we do not focus on construction of blue-noise point sets, but develop a theoretical framework to obtain perceptually pleasing distribution of error in screen space for rendering purposes.

Blue-noise error distribution. Mitchell [1991] observed that blue noise is a desirable property for spectrally optimal ray tracing. Georgiev and Fajardo [2016] were the first to apply results from halftoning literature to screen space-error redistribution for path tracing. The resulting perceptual quality improvements are substantial for smooth enough integrands.

Motivated by the results of Georgiev and Fajardo [2016], Heitz and Belcour [2019] devised a technique aiming to directly optimize the error distribution instead of operating on sample distributions. Their pixel permutation strategy fits the initially white-noise pixel intensities to a prescribed blue-noise mask. This approach scales well with sample count and dimensionality, though the error distribution quality is limited by the fitting to a specific mask and degrades to white noise near geometry discontinuities, unlike the methods of Georgiev and Fajardo [2016] and Heitz et al. [2019].

We propose a perceptual error framework based on an expressive model that unifies these prior methods, providing insight into their (implicit) assumptions and guidelines to alleviate some of their drawbacks. Our general perceptual error formulation does not rely on a target (blue-noise) mask.

3 PERCEPTUAL ERROR MODEL

Our goal is to produce Monte Carlo renderings that, at a fixed sampling rate, are perceptually as close to the ground truth as possible. This requires formalizing the perceptual image error along with an optimization problem that minimizes it. In this section, we build a perceptual model upon the extensive studies done in halftoning

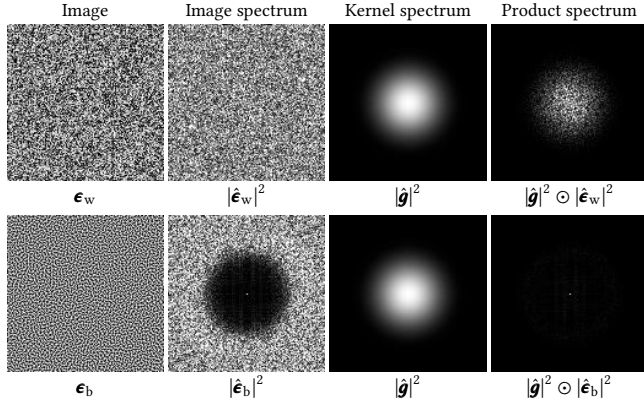


Fig. 2. Error images ϵ_w and ϵ_b with respective white-noise, $|\hat{\epsilon}_w|^2$, and blue-noise, $|\hat{\epsilon}_b|^2$, power spectra. For a low-pass kernel \mathbf{g} modeling the PSF of the HVS (here a Gaussian with std. dev. $\sigma = 1$), the product of its spectrum $|\hat{\mathbf{g}}|^2$ with $|\hat{\epsilon}_b|^2$ has lower magnitude than the product with $|\hat{\epsilon}_w|^2$. This corresponds to lower perceptual sensitivity to ϵ_b , even though ϵ_w has the same amplitude as it is obtained by randomly permuting the pixels of ϵ_b .

literature. We will discuss how to efficiently solve the resulting optimization problem in Section 4.

Given a ground-truth image I and its quantized or noisy approximation Q , we denote the signed error image by:

$$\epsilon = Q - I. \quad (1)$$

It is useful to quantify the error as a single number. A common approach is to take the \mathcal{L}_1 , \mathcal{L}_2 , or \mathcal{L}_∞ norm of ϵ . Such vector norms are permutation-invariant, i. e., they account for the *magnitudes* of individual pixel errors but not for their *distribution* over the image. This distribution is an important factor for the perceived fidelity, since contrast perception is an inherently spatial characteristic of the HVS (Section 2.3).

3.1 Motivation

Several metrics have been proposed in halftoning literature to capture the human perception of image error. Such metrics model the processing done by the HVS as a convolution of the error image ϵ with a kernel \mathbf{g} (see notation in Table 1):

$$E = \|\mathbf{g} * \epsilon\|_2^2 = \|\hat{\mathbf{g}} \odot \hat{\epsilon}\|_2^2 = \langle |\hat{\mathbf{g}}|^2, |\hat{\epsilon}|^2 \rangle. \quad (2)$$

The convolution is equivalent to the element-wise product of the corresponding Fourier spectra $\hat{\mathbf{g}}$ and $\hat{\epsilon}$, whose 2-norm is in turn equal to the inner product of the power spectra images $|\hat{\mathbf{g}}|^2$ and $|\hat{\epsilon}|^2$. Sullivan et al. [1991] minimized the error (2) w.r.t. a kernel \mathbf{g} that approximates the HVS’s modulation transfer function $|\hat{\mathbf{g}}|$ (MTF) [Daly 1987]. Analoui and Allebach [1992] used a similar model in the spatial domain where the kernel approximates the PSF of the human eye.

Convoluting the error image with a kernel incorporates both the magnitude and the distribution of the error into the resulting metric E . In general, the kernel \mathbf{g} can have arbitrary form and characteristics; we assume it represents the HVS PSF. As we discuss in Section 2.3, the HVS sensitivity to a spatial signal can be well approximated by a low-pass filter. Optimizing the error image ϵ to

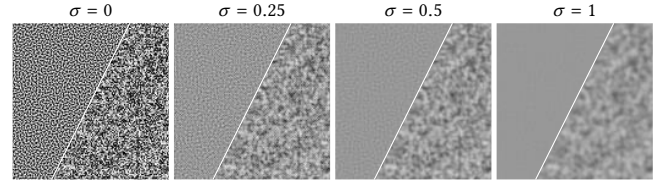


Fig. 3. The appearance of blue noise (**left** images) converges to a constant image faster than white noise (**right** images) with increasing observer distance, simulated here by the standard deviation σ of a Gaussian kernel.

minimize the cost (2) w.r.t. a low-pass kernel would then naturally yield a blue-noise¹ error distribution (see Fig. 2). Consequently, such a distribution can be seen as a byproduct of such optimization, which pushes the spectral components of the error to frequencies least visible to the human eye. To better understand the spatial aspects of contrast sensitivity in the HVS, the MTF (magnitude of the PSF Fourier transform) is usually modeled over a range of viewing distances [Daly 1993]. This is done to account that with increasing viewer distance, spatial frequencies in the image are projected into higher spatial frequencies in the retina. These eventually become invisible, filtered out by the PSF that expands its corresponding kernel in image space. We recreate this experiment to understand the impact of distance over the nature of the error distribution (blue vs. white noise). In Fig. 3, we convolve white- and blue-noise distributions with a Gaussian kernel. Increasing the kernel’s standard deviation corresponds to increasing the distance between observer and screen. The blue-noise distribution reaches a homogeneous state (where the image tone is indiscernible) faster compared to white noise. In the context of rendering, this is equivalent to blue-noise error becoming indiscernible at smaller distances (or smaller denoising low-pass filters) compared to white-noise error. Consequently, a smaller kernel (i. e., viewing distance) allows preserving more image details while removing the noise, for an optimized error distribution.

3.2 Our model

In rendering, the value of each pixel i is estimated via point sampling. Its signed error is thus a function of the sample set S_i used for its estimation: $\epsilon_i(S_i) = Q_i(S_i) - I_i$, where Q_i is the pixel estimate and I_i is the reference (i. e., ground-truth) pixel value. The error of the entire image can be written in matrix form, similarly to Eq. (1):

$$\epsilon(\mathbf{S}) = \mathbf{Q}(\mathbf{S}) - I, \quad (3)$$

where $\mathbf{S} = \{S_1, \dots, S_N\}$ is an “image” containing the sample set for each of the N pixels. With these definitions, we can express the perceptual error in Eq. (2) for the case of Monte Carlo rendering as a function of the sample-set image \mathbf{S} :

$$E(\mathbf{S}) = \|\mathbf{g} * \epsilon(\mathbf{S})\|_2^2, \quad (4)$$

where \mathbf{g} is a given kernel, e. g., the PSF of the HVS.

Our goal is to minimize the energy in Eq. (4). We formulate it as an optimization problem:

¹The term “blue noise” is often used loosely to refer to any spectrum with minimal low-frequency content and no concentrated energy spikes.

$$\arg \min_{\mathbf{S} \in \Omega} \|\mathbf{g} * \epsilon(\mathbf{S})\|_2^2. \quad (5)$$

The solution \mathbf{S} produces an image estimate $\mathbf{Q}(\mathbf{S})$ that is closest to the reference \mathbf{I} w.r.t. the kernel \mathbf{g} . The search space Ω is the set of all possible locations for every sample of every pixel.

Note that the classical MSE metric corresponds to using a zero-width (i. e., one-pixel) kernel \mathbf{g} in Eq. (4). However, the MSE accounts only for the magnitude of the error ϵ , while using wider kernels (such as the PSF) accounts for both magnitude and distribution. Consequently, while the MSE can be minimized by optimizing pixels independently, minimizing the perceptual error requires spatial coordination. In the following section, we devise practical strategies for solving this optimization problem.

4 DISCRETE OPTIMIZATION

The search space in Eq. (5) for each sample set of every pixel is a high-dimensional unit hypercube. Each point in this so-called primary sample space maps to a light transport path in the scene [Pharr et al. 2016]. Optimizing for the sample-set image \mathbf{S} thus entails evaluating the contributions $\mathbf{Q}(\mathbf{S})$ of all corresponding paths. This evaluation is costly, and for any non-trivial scene, \mathbf{Q} is an unpredictable function with many discontinuities. This precludes us from studying all (uncountably infinite) sample locations in practice.

To make the problem tractable, we restrict the search in each pixel to a finite number of (pre-defined) sample sets.² We devise two variants of the resulting discrete optimization problem, which differ in their definition of the search space Ω . In the first variant, each pixel has a separate list of sample sets to choose from (“vertical” search space). The setting is similar to that of (multi-tone) halftoning [Lau and Arce 2007], which allows us to import classical optimization techniques from that field, such as mask-based dithering, error diffusion, and iterative minimization. In the second variant, each pixel has one associated sample set, and the search space comprises permutations of these assignments (“horizontal” search space). We develop a greedy iterative optimization method for this second variant.

In contrast to halftoning, in our setting the ground-truth image \mathbf{I} , required to compute the error ϵ during optimization, is not readily available. We describe our algorithms assuming the ground truth is available, and then discuss how to substitute it with a surrogate to make the algorithms practical.

4.1 Vertical search space

Our first variant considers a *vertical* search space where the sample set for each of the N image pixels is one of M given sets:

$$\Omega = \{\mathbf{S} = \{S_1, \dots, S_N\} : S_i \in \{S_{i,1}, \dots, S_{i,M}\}\}. \quad (6)$$

The objective is to find a sample set for every pixel such that all resulting pixel estimates together minimize the perceptual error (4). This is equivalent to directly optimizing over the M possible estimates $Q_{i,1}, \dots, Q_{i,M}$ for each pixel i , with $Q_{i,j} = Q_i(S_{i,j})$. These estimates can be obtained by, e. g., rendering a stack of M images

²A more general formulation could operate on individual samples, without grouping them into per-pixel sets; we leave this study to future work.

$\mathbf{Q}_j = \{Q_{1,j}, \dots, Q_{N,j}\}$, with $j = 1..M$. The resulting minimization problem reads

$$\arg \min_{\mathbf{O}: O_i \in \{Q_{i,1}, \dots, Q_{i,M}\}} \|\mathbf{g} * (\mathbf{O} - \mathbf{I})\|_2^2. \quad (7)$$

The problem in Eq. (7) is almost identical to that in multitone halftoning. The only difference is that in our setting the “quantization levels”, i. e., the pixel estimates, are non-uniform and differ from pixel to pixel as they are not pre-defined but are the result of point-sampling a spatially varying light-transport integral. This similarity allows us to directly apply existing optimization techniques from halftoning [Lau and Arce 2007]. We consider three such methods, which we outline in Alg. 1 and describe next.

Iterative minimization. Some halftoning methods aim to solve the problem (7) directly via iterative greedy minimization [Analoui and Allebach 1992; Pappas and Neuhoff 1999]. After initializing each pixel to a random quantization level, our implementation traverses the image in serpentine order (as is standard practice in halftoning) and for each pixel picks the level that minimizes the energy. Several full-image iterations are performed; in our experiments convergence to a local minimum is achieved within 10–20 iterations. As a further improvement, the optimization can be terminated when the perceptual error reduction rate falls below a certain threshold or when no estimates are updated within one full iteration. Random pixel traversal order allows terminating at any point but converges slightly slower.

Error diffusion. A classical halftoning algorithm, error diffusion scans the image pixel by pixel, snapping each to the closest quantization level and distributing the resulting error to yet unprocessed nearby pixels according to a given diffusion kernel κ [Floyd and Steinberg 1976]. In our setting, this can be interpreted as using a kernel (κ) that is learned over a specific class of functions, such that the result of error diffusion approximately implies minimizing Eq. (7) [Hocevar and Nizer 2008]. For color images, the Euclidean distance in a relevant color space can be used to find the closest quantization level.

Dither masks. An efficient halftoning approach is to quantize pixel values using thresholds stored in a pre-computed dither mask (or matrix) [Spaulding et al. 1997]. For each pixel, the closest lower and higher (in terms of brightness) quantization levels to the reference value are found, and one of the two is chosen based on the threshold associated with the pixel. This aims to transfer the spectral characteristics of the mask to the error distribution of the dithered image. In a blue-noise mask, neighboring pixels have very different thresholds, leading to a visually pleasant high-frequency output error distribution. Following Eq. (7), here the minimization involves two parts. First, the pre-processing step (performed offline) that involves minimizing $\arg \min_{\mathbf{B}} \|\mathbf{g} * \mathbf{B}\|_2^2$ to obtain a mask \mathbf{B} using \mathbf{g} , which is equivalent to the problem in Eq. (7) with a linear integrand and $\mathbf{I} = \mathbf{0}$. Secondly, the simplified energy $\|\mathbf{O} - \mathbf{I} - f(\mathbf{B})\|$ is minimized, which can be done efficiently through sorting. Here f

Algorithm 1. Three algorithms to (approximately) solve the problem associated with a *vertical* search space (7), producing an output image $\mathbf{O} = \{O_1, \dots, O_N\}$ given a reference image \mathbf{I} and a stack of initial estimates $\mathbf{Q}_1, \dots, \mathbf{Q}_M$. Our iterative minimization scheme updates pixels repeatedly, for each picking the estimate that minimizes the perceptual error (4). Error diffusion quantizes each pixel to the closest estimate, distributing the error to its neighbours based on a kernel κ . Dithering quantizes each pixel in \mathbf{I} based on thresholds in a dither mask \mathbf{B} (optimized w.r.t. the kernel \mathbf{g}).

```

1: function ITERATIVEMINIMIZATION( $\mathbf{g}, \mathbf{I}, \mathbf{Q}_1, \dots, \mathbf{Q}_M, \mathbf{O}, T$ )
2:    $\mathbf{O} \leftarrow \{Q_{1,\text{rand}} \dots, Q_{N,\text{rand}}\}$    ← Init each pixel to random estimate
3:   for  $T$  iterations do
4:     for pixel  $i = 1..N$  do           ← E. g., random or serpentine order
5:       for estimate  $Q_{i,j} \in \{Q_{i,1}, \dots, Q_{i,M}\}$  do
6:         if  $O_i = Q_{i,j}$  reduces  $\|\mathbf{g} * (\mathbf{O} - \mathbf{I})\|_2^2$  then
7:            $O_i \leftarrow Q_{i,j}$            ← Update estimate

8: function ERRORDIFFUSION( $\kappa, \mathbf{I}, \mathbf{Q}_1, \dots, \mathbf{Q}_M, \mathbf{O}$ )
9:    $\mathbf{O} \leftarrow \mathbf{I}$                        ← Initialize solution to reference
10:  for pixel  $i = 1..N$  do                 ← E. g., raster or serpentine order
11:     $O_i^{\text{old}} \leftarrow Q_i$ 
12:     $O_i \in \arg \min_{Q_{i,j}} \|O_i^{\text{old}} - Q_{i,j}\|_2^2$ 
13:     $\epsilon_i \leftarrow O_i^{\text{old}} - O_i$        ✓ Diffuse error  $\epsilon_i$  to yet unprocessed neighbors
14:    for unprocessed pixel  $k$  within support of  $\kappa$  around  $i$  do
15:       $O_k \leftarrow O_k + \epsilon_i \cdot \kappa_{k-i}$ 

16: function DITHERING( $\mathbf{B}, \mathbf{I}, \mathbf{Q}_1, \dots, \mathbf{Q}_M, \mathbf{O}$ )
17:  for pixel  $i = 1..N$  do                 ✓ Find tightest interval  $[Q_i^{\text{low}}, Q_i^{\text{high}}]$ 
18:     $Q_i^{\text{low}} \leftarrow \arg \max_{Q_{i,j}: |Q_{i,j}| \leq |I_i|} |Q_{i,j}|$            containing  $I_i$ 
19:     $Q_i^{\text{high}} \leftarrow \arg \min_{Q_{i,j}: |Q_{i,j}| > |I_i|} |Q_{i,j}|$ 
20:    if  $|I_i| - |Q_i^{\text{low}}| < B_i \cdot (|Q_i^{\text{high}}| - |Q_i^{\text{low}}|)$  then
21:       $O_i \leftarrow Q_i^{\text{low}}$            ✓ Quantize  $I_i$  to  $Q_i^{\text{low}}$  or  $Q_i^{\text{high}}$  using threshold  $B_i$ 
22:    else
23:       $O_i \leftarrow Q_i^{\text{high}}$ 

```

is a monotonic mapping, and different choices result in different algorithms (see more details in Section 7 in the supplemental).

4.2 Horizontal search space

We now describe the second *horizontal* discrete variant of our minimization formulation (5). It considers a single sample set S_i assigned to each of the N pixels, all represented together as a sample-set image \mathbf{S} . The search space comprises all possible permutations $\Pi(\mathbf{S})$ of these assignments:

$$\Omega = \Pi(\mathbf{S}), \text{ with } \mathbf{S} = \{S_1, \dots, S_N\}. \quad (8)$$

The goal is to find a permutation $\pi(\mathbf{S})$ that minimizes the perceptual error (4). The optimization problem (5) thus takes the form

$$\arg \min_{\pi(\mathbf{S}) \in \Pi(\mathbf{S})} E(\pi(\mathbf{S})) = \arg \min_{\pi(\mathbf{S}) \in \Pi(\mathbf{S})} \|\mathbf{g} * (\mathbf{Q}(\pi(\mathbf{S})) - \mathbf{I})\|_2^2. \quad (9)$$



Algorithm 2. Given a convolution kernel \mathbf{g} , a reference image \mathbf{I} , an initial pixel sample-set assignment \mathbf{S} , and an image estimated with that assignment $\mathbf{Q}(\mathbf{S})$, our greedy sample relocation algorithm iteratively swaps pixel assignment to minimize the perceptual error E_{Δ} (10), producing a permutation π of the sample-set assignment.

```

1: function ITERATIVEMINIMIZATION( $\mathbf{g}, \mathbf{I}, \mathbf{S}, \mathbf{Q}(\mathbf{S}), T, R, \pi$ )
2:    $\pi \leftarrow$  identity permutation       ← Initialize solution permutation
3:   for  $T$  iterations do
4:     for pixel  $i = 1..N$  do           ← E. g., random or serpentine order
5:        $\pi'_i \leftarrow \pi$              ✓ Find best pixel in neighborhood to swap with
6:       for pixel  $j$  in  $(2R+1)^2$  neighborhood centered at  $i$  do
7:         if  $E_{\Delta}(\pi_{i \leftrightarrow j}(\mathbf{S})) < E_{\Delta}(\pi'(\mathbf{S}))$  then           ← Eq. (10)
8:            $\pi'_i \leftarrow \pi_{i \leftrightarrow j}$            ← Accept swap as current best
9:        $\pi \leftarrow \pi'$ 

```

We can explore the permutation space $\Pi(\mathbf{S})$ by swapping the sample-set assignments between pixels. The minimization requires updating the image estimate $\mathbf{Q}(\pi(\mathbf{S}))$ for each permutation $\pi(\mathbf{S})$, i. e., after each swap. Such updates are costly as they involve multiple ray-tracing operations for each of potentially millions of swaps. We need to eliminate these extra rendering invocations during the optimization to make it practical. To that end, we observe that for pixels solving similar light-transport integrals, swapping their sample sets gives a similar result to swapping their estimates. We therefore restrict the search space to permutations that can be generated through swaps between such pixels. This enables efficient optimization by directly swapping the pixel estimates of an initial rendering $\mathbf{Q}(\mathbf{S})$.

Error decomposition. Formally, we express the estimate produced by a sample-set permutation in terms of permuting the pixels of the initial rendering: $\mathbf{Q}(\pi(\mathbf{S})) = \pi(\mathbf{Q}(\mathbf{S})) + \Delta$. The error Δ is zero when the swapped pixels solve the same integral(s). Substituting into Eq. (9), we can approximate the perceptual error by (see derivation in Appendix A)

$$\begin{aligned} E(\pi(\mathbf{S})) &= \|\mathbf{g} * (\pi(\mathbf{Q}(\mathbf{S})) - \mathbf{I} + \Delta)\|_2^2 & (10) \\ &\approx \|\mathbf{g} * (\pi(\mathbf{Q}(\mathbf{S})) - \mathbf{I})\|_2^2 + \|\mathbf{g}\|_1^2 \sum_i d(i, \pi(i)) = E_{\Delta}(\pi(\mathbf{S})). \end{aligned}$$

In the approximation E_{Δ} , the term $d(i, \pi(i))$ measures the dissimilarity between pixel i and the pixel $\pi(i)$ it is relocated to by the permutation. The purpose of this metric is to predict how different we expect the result of re-estimating the pixels after relocating their sample sets to be compared to directly relocating their initial estimates. It can be constructed based on assumptions or knowledge about the image, e. g., coming from auxiliary buffers (depth, normals, etc).

Local similarity assumption. In our implementation we use a simple binary dissimilarity function returning zero when i and $\pi(i)$ are within some distance r and infinity otherwise. We set r between 1 and 3; it should ideally be locally adapted to the image smoothness/regularity. This allows us to restrict the search space $\Pi(\mathbf{S})$ only to permutations that swap adjacent pixels where it is more likely that Δ is small.

Iterative minimization. We devise a greedy iterative minimization scheme for this variant similar in spirit to the iterative minimization in Alg. 1. Given an initial image estimate $\mathbf{Q}(\mathbf{S})$ produced by randomly assigning a sample set to every pixel, our algorithm iterates over all pixels and for each considers swaps within a $(2R+1)^2$ neighborhood; we use $R = 1$. The swap that brings the largest reduction in the perceptual error E_{Δ} is accepted. Several full-image iterations are performed. Algorithm 2 provides pseudo code. We use $T = 10$ iterations in our experiments. The algorithm could be terminated based on the perceptual error or swap reduction rate. Additionally, the algorithm can be sped up considerably by using optimizations applicable to our energy (see supplemental Section 5).

The parameter R controls the trade-off between the cost of one iteration and the amount of exploration it can do. Note that this parameter is different from the maximal relocation distance r in the dissimilarity metric, and also $R \leq r$.

Due to the pixel (dis)similarity assumptions, the optimization can produce some mispredictions, i. e., it may swap the estimates of pixels for which swapping the sample sets produces a significantly different result. Thus $\pi(\mathbf{Q}(\mathbf{S}))$ cannot be used as a final image estimate. We therefore re-render the image with the optimized permutation π to obtain the final estimate $\mathbf{Q}(\pi(\mathbf{S}))$.

4.3 Discussion

Practical algorithms can be classified based on the choice of search space (*horizontal* versus *vertical*) and optimization strategy (iterative, error diffusion, dithering). The above choices affect the overall quality and speed of algorithms.

Search space. Discretizing the search space Ω makes the optimization problem (5) tractable. To make it truly practical, it is necessary to avoid repeated image estimation (i. e., $\mathbf{Q}(\mathbf{S})$ evaluation) during the search for the solution \mathbf{S} . Our *vertical* (7) and *horizontal* (9) optimization variants are formulated specifically with this goal in mind. All methods in Algs. 1 and 2 operate on pre-generated image estimates that constitute the solution search space.

Our *vertical* formulation takes a set of M input estimates $\{Q_{i,j} = Q_i(S_{i,j})\}_{j=1}^M$ for every pixel i , one for each sample set $S_{i,j}$. Noting that $Q_{i,j}$ are MC estimates of the true pixel value, this set can be cheaply expanded to a size as large as $2^M - 1$ by also considering the average of the estimates in each of its subsets (excluding the empty subset). In practice only a fraction of these subsets can be used, since the size of the power set grows exponentially with M .

In contrast, our *horizontal* formulation builds a search space given just a single input estimate Q_i per pixel i . We consciously restrict the space to permutations between nearby pixels, so as to leverage local pixel similarity and avoid repeated pixel evaluation. The disadvantage of this approach is that it requires re-rendering the image after optimization, with unpredictable results (mispredictions) that can lead to local degradation of image quality. Additionally, while some halftoning methods (iterative energy minimization and versions of dither matrix halftoning) can be adapted to this search space, it is non-trivial to find straightforward reformulations for other algorithms (e. g., error diffusion).

It is also possible to combine our two formulations into a hybrid one that takes one input estimate per pixel but considers a separate

search space for each pixel, constructed by borrowing neighboring estimates.

Optimization strategy. Another important design decision is the choice of optimization method. For the *vertical* formulation, iterative methods provides the most flexibility, control, and quality, but are most computationally expensive. In contrast, error diffusion and dither-mask halftoning can be seen as only approximately solving the optimization problem (7), yielding results of a lower quality. An important difference between classical halftoning and our extension is the fact that quantization levels differ between pixels. This makes the gap in quality between image-adaptive (iterative, error diffusion) and non-adaptive (dither-mask halftoning) methods even larger. Additionally, in the classical MC rendering setting, iterative and error-diffusion methods handle color natively, while dither-mask halftoning requires greyscale input. While this can be mitigated by modifying the renderer or by extending the dithering through algorithms such as bipartite Euclidean matching, this comes at both a performance and quality cost compared to iterative and error diffusion algorithms. The main advantage of dither-mask halftoning over error diffusion in our setting is that the former involves the kernel \mathbf{g} explicitly, while error diffusion relies on a diffusion kernel $\mathbf{\kappa}$ that cannot be related directly to \mathbf{g} .

Surrogate for reference image. All our formulations depend on the reference image \mathbf{I} which is unknown, unlike in halftoning. To that end, the reference can be substituted with an approximation, i. e., *surrogate* image, \mathbf{I}' , which can be obtained, e. g., via (ideally feature-preserving) filtering of an estimate \mathbf{Q} . We will discuss surrogates in more detail in Sections 7.1 and 7.3, but it is important to point out that *all* existing methods rely on a surrogate whether explicitly or implicitly.

5 A-POSTERIORI & A-PRIORI METHODS

In our framework, the histogram sampling approach of Heitz and Belcour [2019] classifies as a *vertical* method, and their permutation approach as a *horizontal* method. Both these methods employ variants of dither-mask halftoning. We next show that in both cases, their algorithms rely on implicitly constructed surrogates.

5.1 Implicit surrogates in a-posteriori approaches

All existing error distribution methods rely on an implicit surrogate. For the histogram method of Heitz and Belcour [2019], since the mean value of the blue-noise mask maps to the median of the estimates, the implicit surrogate is the median of the sorted estimates in each pixel. Furthermore, the histogram method can pick any of the estimates within a pixel—unlike classical halftoning that samples the closest lower and higher quantization level [Spaulding et al. 1997]—which results in a higher error amplitude. Consequently, pixels for which the mask value deviates strongly from the mean value could end up with outliers leading to fireflies in the rendered image, even if those were not present in the averaged image (Fig. 7).

The permutation method of Heitz and Belcour [2019], on the other hand, has a piecewise constant implicit surrogate. We show this formally in the supplemental document (supplemental, Section 7). In words, the permutation method uses a sorting pass which minimizes

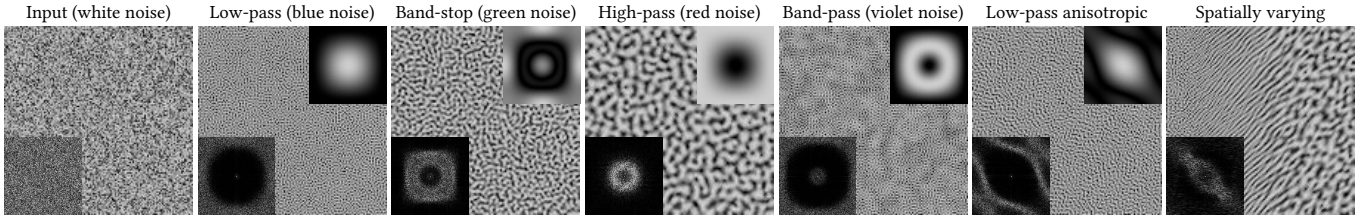


Fig. 4. Using our formulation (5), the distribution of an input error image can be optimized w.r.t. arbitrary kernels. Here we have modified our relocation algorithm (Section 4.2) to directly swap the pixels of the input image. Insets show the power spectra of the kernels (top right) and the images (bottom left).

the \mathcal{L}_2 distance between the pixel values and the dither mask within each tile. This transfers the *blue-noise* characteristics of the dither mask to the *signal*. However, the actual goal is to transfer these spectral characteristics to the *error*, not the *signal*. For the two to be equivalent, the *signal* within each tile needs to be assumed constant. And indeed, a constant offset does not change the minimizer of the energy which sorting minimizes. This implies that the implicit surrogate in this case is a piecewise constant function within each tile. Our framework, however, uses an explicit surrogate that allows full control over the quality of error distribution.

5.2 A-priori methods

By making simplifying assumptions about \mathbf{I} and \mathbf{Q} , our sample relocation algorithm could be used with no actual knowledge about the image. For example, assuming that every pixel solves the same integral turns \mathbf{I} into a constant image and makes the error term Δ in Eq. (10) vanish. This allows us to swap any two pixels and simplifies the perceptual error to $E(\pi(\mathbf{S})) = \|\mathbf{g} * \pi(\boldsymbol{\epsilon}(\mathbf{S}))\|_2^2$. Further assuming a simple analytic shape for the pixel integrand, the per-pixel error image $\boldsymbol{\epsilon}(\mathbf{S})$ can be quickly rendered once and the perceptual optimization performed by simply swapping its pixels. In this formulation, prior methods correspond to using a (family of) step function(s) [Heitz et al. 2019] or a class of functions mapping far away samples to far away values [Georgiev and Fajardo 2016] for the integrand, respectively. This approach, coined “a-priori” by Heitz and Belcour [2019], is practical but its output fidelity is limited by lack of adaptivity resulting from its strong assumptions.

Our framework unifies the a-priori and a-posteriori approaches, showing that the two lie on a continuum (supplemental Section 2). In our framework, the “a-priori” method of Heitz et al. [2019] tries to simultaneously minimize for a large number of simple integrands while the search space is restricted to the ranking and scrambling keys of a Sobol sequence. This roughly corresponds to a *vertical* and *horizontal* search space, respectively. At the same time, we note that the energy that is used is empirically motivated, but it can be made to agree with our perceptually motivated energy by simply absorbing the Gaussian convolution within the \mathcal{L}_2 norm.

Similarly, the method of Georgiev and Fajardo [2016] consisting of toroidally shifting a sequence by a mask, can also be cast in our framework provided that the mask is optimized w.r.t. our energy with an appropriate set of integrands. Even if motivated purely empirically, the energy in the paper can be related to our energy if a whole class of integrands is considered where faraway samples are mapped into faraway values. We also note that the toroidal shift

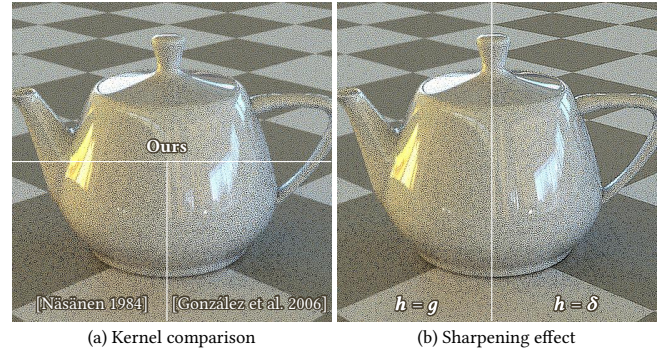


Fig. 5. (a) Comparison of our Gaussian kernel \mathbf{g} against those of Näsänen [1984] and González et al. [2006]. (b) Sharpening effect of setting the reference-image kernel \mathbf{h} to the zero-width Kronecker $\boldsymbol{\delta}$ kernel in Eq. (13).

degrades the quality of the optimized mask and consequently the quality of the blue noise (see supplemental Section 8).

6 EXTENSIONS

Our perceptual error formulation (4) considers some image distortions due to the CSF but not all. The HVS applies additional, localized and non-linear processing to the input signal. We analyze different aspects of the model and devise three extensions that capture more effects.

Kernels and PSFs. In Fig. 5a, we compare different PSF models (i. e., low-pass kernels) from halftoning literature [Näsänen 1984; González et al. 2006]. In our experiments, we use a binomial kernel that approximates a Gaussian kernel [Papoulis and Pillai 2002]; it is cheap to evaluate and performs on par with these state-of-the-art PSFs.

We further analyze kernels with band-stop, high-pass, band-pass, and anisotropic spectral characteristics in Fig. 4. Starting from a white-noise error distribution (i. e., with a uniform random value in $[-0.5, 0.5]$ assigned to each pixel), our *horizontal* iterative minimization algorithm is able to optimize the shape of the noise to produce the inverse behaviour to the kernel in the spectral domain. The rightmost image in Fig. 4 illustrates the result from using such a spatially varying kernel produced from the convex combination of a binomial and an anisotropic high-pass kernel, with the interpolation parameter varying horizontally across the image. Our algorithm can well adapt the noise shape based on the kernel.

Tone reproduction. Considering that the rendered image will be viewed on a medium with limited dynamic range (e. g., screen or paper), we can incorporate a tone mapping operator \mathcal{T} into the perceptual error:

$$E(\mathbf{S}) = \|\mathbf{g} * (\mathcal{T}(\mathbf{Q}(\mathbf{S})) - \mathcal{T}(\mathbf{I}))\|_2^2. \quad (11)$$

Doing this also bounds the per-pixel error: $\boldsymbol{\epsilon}(\mathbf{S}) = \mathcal{T}(\mathbf{Q}(\mathbf{S})) - \mathcal{T}(\mathbf{I})$, suppressing pixel outliers and making the optimization more robust in scenes with high dynamic range.

Chromatic noise. While the HVS reacts more strongly to luminance compared to color, ignoring chromaticity entirely can have a negative effect on the distribution of color noise in the image. To mitigate this, one can penalize each color channel c separately:

$$E(\mathbf{S}) = \sum_{c \in \{r, g, b\}} \lambda_c \|\mathbf{g}_c * (\mathbf{Q}_c(\mathbf{S}) - \mathbf{I}_c)\|_2^2. \quad (12)$$

where λ_c is a weight parameter. In our experiments (Section 7), we set $\lambda_c = 1$ and use the same kernel \mathbf{g}_c for every channel. It is, however, possible to consider a more appropriate color space than RGB (e. g., YCbCr). In such case, per-channel kernels may differ [Sullivan et al. 1991].

Observer-screen distance. Being based on the perceptual models of the HVS [Sullivan et al. 1991; Analoui and Allebach 1992], our formulation (4) assumes that the estimate \mathbf{Q} and the reference \mathbf{I} are viewed from the same (range of) distance(s). The viewing distances can be decoupled by applying different kernels to \mathbf{Q} and \mathbf{I} :

$$E(\mathbf{S}) = \|\mathbf{g} * \mathbf{Q}(\mathbf{S}) - \mathbf{h} * \mathbf{I}\|_2^2. \quad (13)$$

Minimizing this error makes \mathbf{Q} appear, from some distance $d_{\mathbf{g}}$, similar to \mathbf{I} seen from a different distance $d_{\mathbf{h}}$. The special case of using a Kronecker delta kernel $\mathbf{h} = \boldsymbol{\delta}$ (i. e., with the reference \mathbf{I} seen from up close) yields $E(\mathbf{S}) = \|\mathbf{g} * \mathbf{Q}(\mathbf{S}) - \mathbf{I}\|_2^2$, which has been shown to have an edge enhancing effect in halftoning [Anastassiou 1989; Pappas and Neuhoff 1999]. We demonstrate this effect in Fig. 5b. We use $\mathbf{h} = \boldsymbol{\delta}$ for all our experiments in Section 7.

7 EXPERIMENTS

In this section, we detail our testing methodology and present empirical results employing our proof-of-concept algorithms. We render several scenes using our iterative energy minimization, error diffusion, and dither matrix halftoning approaches and compare against the histogram and permutation methods of Heitz and Belcour [2019]. The quantitative analysis is performed in Table 2 over all the methods, and the runtime for the optimization can be found in Table 3.

7.1 Setup

Energy formulation. We use the perceptual model $\|\mathbf{g} * \mathbf{Q}(\mathbf{S}) - \mathbf{h} * \mathbf{I}\|_2^2$ with $\mathbf{h} = \boldsymbol{\delta}$ from Eq. (13). In our implementation, we tone map (Eq. (11)) the images to match the display and consider all (RGB) channels (Eq. (12)) for both iterative and error diffusion methods. The dithering approach, however, requires solving a bipartite Euclidean matching problem to take into account different channels, thus we consider it only in the greyscale setting, since this allows using sorting for the optimization.

Kernel \mathbf{g} . In all our experiments (except where explicitly mentioned), we use a 3×3 binomial kernel \mathbf{g} which approximates a Gaussian kernel [Lindeberg 1990] with standard deviation $\sigma = 1/\sqrt{2}$. More sophisticated kernels may be used if desired, however, we found that our Gaussian approximation gives satisfactory results (Fig. 5a) in all experiments. The optimal viewing distance corresponding to our kernel is approximately 90cm for a screen with 218 DPI (136 pixels per visual degree).

Rendering setup. All scenes are rendered in PBRTv3 [Pharr et al. 2016] using the path integrator and, occasionally, the bidirectional path tracing integrator. Our methods do not depend on the dimensionality of the problem, however, in order to keep the rendering time reasonable we set the maximum path depth to 5 for all scenes. The reference images are generated using a Sobol sampler with sample counts greater than 1024 samples per pixel. All other images are rendered using a random sampler. In all scenes (except in the animations), we shoot primary rays through the center of the pixel in order to separate the geometry integration from the light transport integration. We also provide animation results in the supplementary data on the following scenes: *Utah Teapot* (360 frames), *Modern Hall* (120 frames), *San Miguel* (120 frames), *Bathroom* (120 frames).

Surrogate construction. To construct a surrogate for our methods, we denoise the averaged image with the Intel Open Image Denoiser [int 2018]. The denoiser’s input is the averaged image, a normal buffer, and a buffer containing the base color of materials where applicable. Heitz and Belcour’s methods use implicit surrogates. We analyze the effect of various surrogates in Fig. 10, and showcase the surrogates generated from the Intel Denoiser in Fig. 11.

Perceptual error metrics. We also evaluate the quality of our results using perceptual metrics like S-CIELAB [Zhang and Wandell 1997] (see supplemental) and HDR-VDP-2 [Mantiuk et al. 2011], with parameters matching our kernel. Among these, HDR-VDP-2 quantifies best the considerable visual improvement due to *a-posteriori* methods. We also include a metric, dubbed *perceptual MSE* (pMSE). It is derived by normalizing our perceptual error Eq. (4) by the pixel count multiplied by the number of channels (with $\mathbf{h} = \boldsymbol{\delta}$). Additionally, to analyze the local blue-noise quality we provide tiled Fourier power spectra (Fig. 1, see supplemental results) of the signed error $\mathbf{Q}(\pi(\mathbf{S})) - \mathbf{I}$ in order to showcase the quality achieved for the distribution of the error as blue noise. The image is split into tiles of size 32×32 and the power spectrum is computed for each tile. For visualization purposes, a logarithmic transform is applied within each tile and the resulting values are normalized so that the highest value is (1, 1, 1). Note that the power spectrum is computed for the *error* w. r. t. the reference image \mathbf{I} and not the surrogate, which quantifies the blue noise distribution objectively.

7.2 Rendering comparisons

Vertical approaches. We compare all three different class of *vertical* methods (Alg. 1): dithering-based, error diffusion using Floyd-Steinberg kernel $\boldsymbol{\kappa}$ [Floyd and Steinberg 1976] and the iterative minimization approach using our kernel \mathbf{g} .

We first compare our iterative minimization approach against the histogram sampling method [Heitz and Belcour 2019] in Fig. 6.



Fig. 6. *Vertical methods*. In the top row, we compare our iterative approach with Histogram sampling method [Heitz and Belcour 2019] over three different scenes: *Modern Hall*, *San Miguel*, *Bathroom*. One estimate from a histogram of 16 (left) or 64 (right) different 1spp estimates is used to render the histogram method. Our approach (middle) uses only 4 primary estimates as search space following Eq. (7) and outperforms both histograms. Bottom row shows a cropped region of the *baseline* averaged image with 4spp. Please zoom-in (or see HTML viewer in the supplement) to appreciate the quality difference.

The histogram sampling approach performs suboptimally compared to our iterative minimization approach even when it is provided with 16 times more samples. This goes to illustrate the fact that it is neither theoretically nor practically optimal, mainly because its dithering and implicit surrogate are suboptimal (see Section 5.1, and supplemental Section 7). In Fig. 7, we perform an *equal sample* comparison for all vertical methods. All our vertical methods consistently outperform the histogram sampling method. This also seems to match the *probability of detection* map from HDR-VDP-2 shown in the bottom row of the figure.

In Fig. 1, we illustrate that denoising artifacts can be removed through our optimization. A white noise image denoised with the Open Intel Image Denoiser results in objectionable artifacts, while performing our optimization subsequently and then denoising, removes those artifacts entirely. In Fig. 1, the denoised version of the averaged image results in conspicuous unpleasant artifacts. Using this image as a surrogate for our method, the optimization finds a subset of unbiased estimates that match the surrogate well in terms of pMSE. Clearly the new image even if constructed from previously unbiased estimates is not fully unbiased, however, the introduced bias allows for more regularity. This regularity pays off since the subsequent denoising does not produce the artifacts which were inherent to the denoised results using the averaged image (where the error distribution was white noise).

Overall, *vertical* approaches generally rank in the following order of increasing visual quality: histogram sampling, our dithering, our error diffusion, our iterative minimization with a stack of 4 estimates, and our iterative minimization with the *powerset* of the estimates (Table 2). For more details and full-size image comparisons we refer the reader to our supplementary HTML material.

Horizontal approaches. We consider two *horizontal* approaches: our iterative energy minimization approach (Alg. 2) and Heitz and Belcour’s permutation approach. For our relocation method, we use a search radius $R = 1$ (Alg. 2) and we allow pixels to travel within a disk neighbourhood centered around the initial pixel location. We set the disk radius r to 1 pixel (Alg. 2), which approximately corresponds to tile size 3 for Heitz and Belcour’s permutation method. For the permutation approach we consider tiles sizes 2 and 8.

Comparisons on the *Modern Hall*, *White Room*, and the *Bathroom* scenes can be found in Fig. 8. The scenes are rendered over 16 frames, and retargeting is applied for Heitz and Belcour’s approach. The scenes are intentionally kept static in order to achieve optimal results for [Heitz and Belcour 2019], nevertheless, the permutation approach’s results remain substantially closer to white noise in distribution. For non-static animation results we refer the reader to the supplementary videos where we have provided several animations. We have tested the permutation approach at tile sizes 2 and 8 and we always include the better image. In all cases the pMSE is 20 to 40 percent lower for our approach compared to the permutation approach (see Table 2), which also agrees with our perceptual evaluation of the images. The error in our images is a lot closer in distribution to high quality blue noise, while in the permutation approach it has stronger white noise characteristics.

In Fig. 9, we perform an *equal sample* comparison of our *vertical* methods with Heitz and Belcour’s permutation approach on the scenes: *Living Room*, *Classroom*, and *Grey Room*. Our vertical methods consistently outperform the permutation approach both in terms of perceptual metrics (Table 2) and our subjective perceptual evaluation.

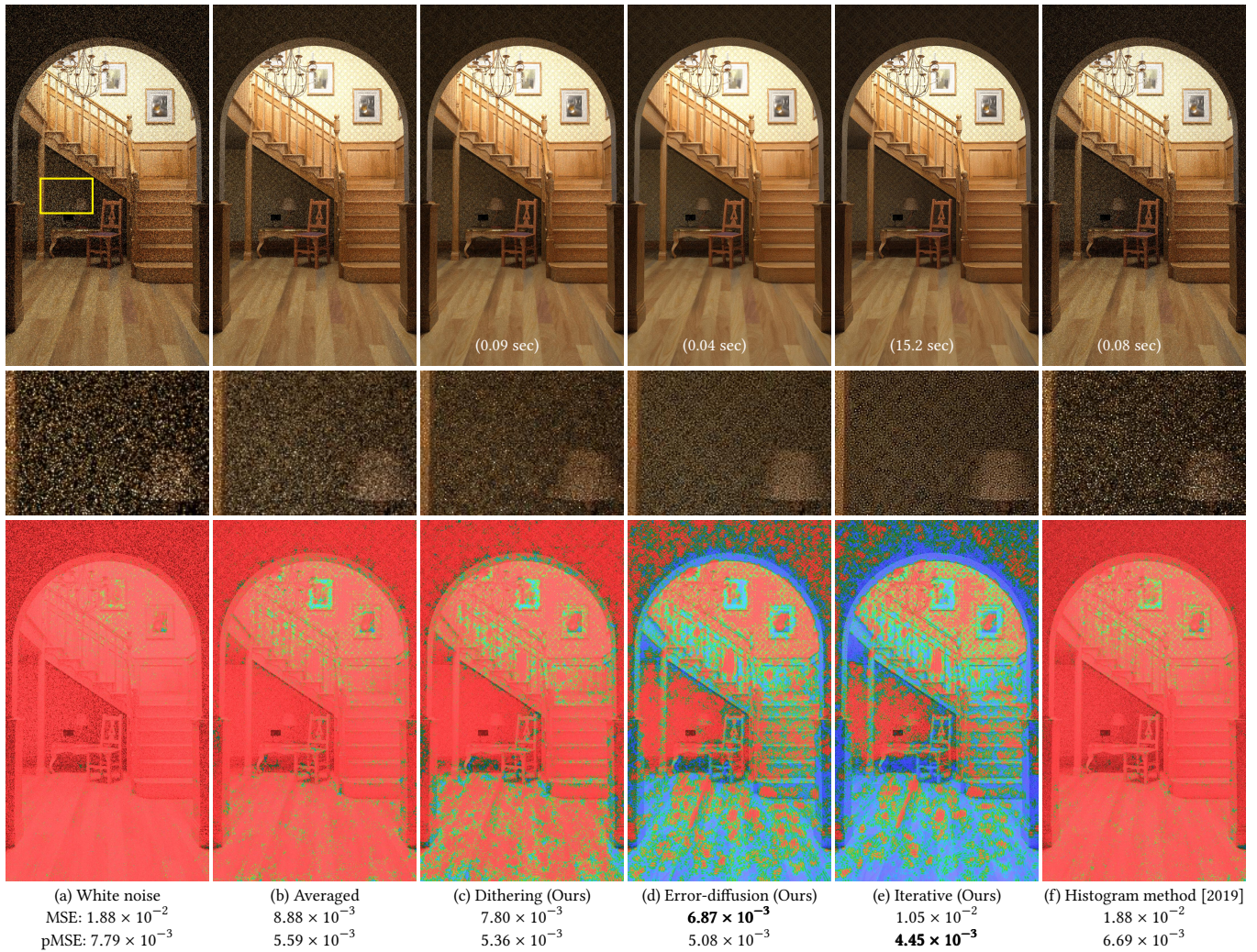


Fig. 7. *Vertical* method comparisons where for each pixel one primary estimate is picked from 4 primary estimates. We compare our three variants: dithering (c), error-diffusion (d) and iterative approach (e) with Histogram sampling method [Heitz and Belcour 2019] (f). Our iterative approach in (e) gives very high quality blue-noise error distribution, marked by the lower pMSE. Our error-diffusion based approach in (d) is computationally fast and has quality comparable to the iterative approach in (e). Our dithering approach (c) shows minor improvement but is still better than the *baseline* averaged image (4spp) even though they do not directly optimize for it. Bottom row shows the detection probability [Mantiuk et al. 2011] which indicates how likely it is for a human observer to notice the difference w.r.t. the reference image (blue refers to lower error) when viewed from the appropriate distance.

Timings. Optimization timings for all approaches can be found in Table 3. Here we discuss some peculiarities of the approaches which affect the runtime. Our error diffusion approach (Alg. 1) is comparable in terms of optimization runtime to dither matrix halftoning based approaches like Heitz and Belcour’s histogram sampling and permutation approaches. In the absence of parallelism, it can often outperform those, since no sorting is required. There are also parallel variants of error diffusion in the literature [Metaxas 2003]. At the same time, the quality of the approach is often comparable to the quality of our iterative energy minimization method.

The methods that provide the best quality and control are also the slowest: our iterative energy minimization approaches. For iterative *vertical* methods we have chosen a maximum of 100 iterations, while usually those converge in about 20. The iterative *horizontal* approach generally cannot fully converge in less than a hundred iterations thus we limit the iterations to $T = 10$ (see the supplemental for an insight on this difference in convergence). This limit does not affect the quality greatly as mispredictions dominate the error for *horizontal* methods. Both methods can be made several orders of magnitude faster if additional optimisations are implemented [Analoui and Allebach 1992; Koge et al. 2014], and we have derived



Fig. 8. We compare our *horizontal* iterative energy minimization (Alg. 2) with Heitz and Belcour’s permutation approach (with retargeting) over a sequence of 16 frames. Top row shows the 1st frame and the bottom row shows the 16-th frame over three different scenes. Our *horizontal* approach consistently outperforms Heitz and Belcour’s permutation approach both qualitatively and quantitatively in terms of pMSE and MSE (see Table 2).

such optimizations in our supplemental (supplemental Section 5). We also note that the runtime scales linearly in the number of pixels of the image multiplied by the number of pixels of the kernel. On the other hand, it doesn’t increase based on the number of samples or the dimensionality of the integrand.

Except for the time required for optimizing the sample sets assignment, our methods rely on an explicit surrogate constructed through the Open Intel Image Denoiser in most of the considered experiments, which for 512×512 images takes about half a second. The surrogate can be constructed through other means as we discuss next.

7.3 Bias analysis

In order to achieve a blue noise error distribution, *a-posteriori* methods introduce varying degrees of bias. For instance, Heitz and Belcour’s approaches can be fully unbiased only if a white noise mask is used. However, the resulting error distribution, in that case, would also be white (MC) noise. Making the mask *correlated* (or *non-random*) allows for a better error distribution at the cost of introducing bias in the end result. Due to the implicit surrogate,

these approaches do not allow for explicit control over the bias, other than modifying the mask to include varying degrees of randomness. Conversely, our approach relies on an explicit surrogate which allows full control over the bias.

We propose different ways to control the amount of bias by: modifying the energy (Appendix B), restricting the search space and limiting the number of iterations for iterative methods. Our iterative energy minimization approaches are able to fit very closely to a surrogate, however, if that surrogate is suboptimal this may be undesirable. In Fig. 10, we perform experiments with several surrogates and extend the energy of Alg. 1 to provide control over the bias (see Appendix B). We can observe that perceptually optimal results are achieved for differing amounts of bias to the surrogate depending on how it was constructed. Notably, with the reference the best result is achieved when maximum bias is allowed. On the other hand, our method with the piecewise tile-constant surrogate requires the amount of bias to be limited in order to remove artifacts due to the surrogate, as can be seen from the third row.



Fig. 9. Quality comparison at equal sample count between our three variants of vertical methods (1/4spp) against Heitz and Belcour’s permutation approach with retargeting (4spp). Since their permutation approach improves visual quality over a sequence of frames, we show the 16-th frame from the sequence. To get better blue-noise error distribution we consider 8×8 tile size for their method. Our vertical methods, however, show improvements from the first frame as shown here. Particularly, our error-diffusion method outperforms their approach in both quality and speed (see Table 2 and Table 3). Bottom row shows the *baseline* averaged (4spp) image.



Fig. 10. Bias analysis. We design different surrogates to analyze their impact on the error distribution. Each column uses a different surrogate. From top to bottom, we vary the bias control parameter: $C = 0$ implies perfect fit to a surrogate whereas $C = 1$ implies otherwise. This showcases that, for poor surrogates, our methods can avoid fitting too closely. We place Heitz and Belcour’s histogram method (in the middle) next to the image that approximately resembles its visual quality. All other images are rendered using one out of the 4 primary estimates per pixel using the iterative *vertical* method. Zoom-in recommended to see the quality difference.



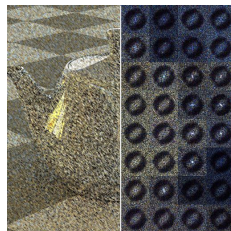
Fig. 11. Here we show the surrogates used for all the scenes. For each scene, the surrogates are generated by denoising the underlying noisy estimate using the Intel Open Image denoiser [int 2018].

8 CONCLUSION AND FUTURE WORK

Our theoretical framework makes an important step towards a formal understanding of the optimality of sample distributions not just w.r.t. numerical integration error but also human perception. We transfer a perceptual kernel-based model from halftoning and adapt it to the context of Monte Carlo rendering.

We formulate an optimization problem that can leverage prior information about the scene. This may be knowledge about the light transport, its dimensionality and smoothness, geometry and textures, or post-processing kernels (e. g., the HVS PSF, or spatially varying denoising kernels). It also provides valuable insights and a formal mathematical framework in which the problem can be studied further.

Our optimization is robust and can also be used to create artistic noise distributions with custom target Fourier power spectra, here showing the SIGGRAPH logo as an example on the right. To obtain the corresponding spatial kernel, we make the logo (greyscale, downscaled) image conjugate symmetric, which ensures that its inverse Fourier transform contains only real values. That inverse, divided by its maximum value, is our optimization kernel g .



Our method is also applicable for progressive and adaptive perceptually optimal rendering, which has only been explored in an a-priori context [Heitz et al. 2019]. Particularly, *vertical* methods can trivially handle a varying number of samples per pixel. Additionally, if samples are sequentially added to the various sample sets from which *vertical* methods choose, then progressive rendering only requires running the optimization every time new samples are introduced.

One promising avenue for future research is incorporating more complex perceptual effects into our error formulation (4), such as visual masking [Bolin and Meyer 1998; Ramasubramanian et al. 1999], as well as more robust metrics than the squared \mathcal{L}_2 norm of a convolution (possibly including nonlinear relationships).

It is also interesting to study the various interactions between our formulation and denoising methods. Ideally, the shape of the (spatially varying) denoising kernels and the error distribution (w.r.t. these kernels) would be optimized simultaneously in a loop, to achieve better image reconstruction for a given sample budget (Fig. 1).

The discrete nature of optimization methods prevents them from exploring the entire, continuous sample space. This seems possible for *a-priori* methods, which could potentially optimize the samples w.r.t. a suitably chosen smooth pixel integrand, e. g., via gradient descent. The same can be done for *a-posteriori* methods if assumptions on the integrands are made, or approximation of the integrands are constructed based on point samples and a class of reconstruction functions. In an a-posteriori setting it would also be interesting to investigate the use of differentiable rendering [Loubet et al. 2019; Zhang et al. 2020].

Finally, we have discussed: energies, search spaces, and optimization strategies for *a-priori* methods as an extension of our formulation for *a-posteriori* methods. We have not evaluated those experimentally however. A promising direction for future research is learning a set of integrands typical for a specific class of scenes. Then those integrands can be used directly in our proposed *a-priori* energy to optimize sequences with desirable integration and spectral properties.

REFERENCES

2018. Intel Open Image Denoise. <https://www.openimagedenoise.org/>.
- J. P. Allebach and B. Liu. 1976. Random quasi-periodic halftone process. *J. Opt. Soc. Am.* 66, 9 (Sep 1976), 909–917. <https://doi.org/10.1364/JOSA.66.000909>
- Mostafa Analoui and Jan P. Allebach. 1992. Model-based halftoning using direct binary search. In *Human Vision, Visual Processing, and Digital Display III*, Bernice E. Rogowitz (Ed.), Vol. 1666. International Society for Optics and Photonics, SPIE, 96 – 108. <https://doi.org/10.1117/12.135959>
- D. Anastassiou. 1989. Error diffusion coding for A/D conversion. *IEEE Transactions on Circuits and Systems* 36, 9 (1989), 1175–1186.
- Peter G.J. Barten. 1999. *Contrast sensitivity of the human eye and its effects on image quality*. SPIE – The International Society for Optical Engineering.
- Barbara E. Bayer. 1973. An optimum method for two-level rendition of continuous-tone pictures. In *Proceedings of IEEE International Conference on Communications, Conference Record*, Vol. 26. 11–15.
- Mark R. Bolin and Gary W. Meyer. 1995. A Frequency Based Ray Tracer. In *SIGGRAPH '95*. 409–418.
- Mark R. Bolin and Gary W. Meyer. 1998. A Perceptually Based Adaptive Sampling Algorithm. In *SIGGRAPH '98*. 299–309.
- A. Celarek, W. Jakob, M. Wimmer, and J. Lehtinen. 2019. Quantifying the Error of Light Transport Algorithms. *Computer Graphics Forum* 38, 4 (2019), 111–121. <https://doi.org/10.1111/cgf.13775>
- Chakravarty R. Alla Chaitanya, Anton S. Kaplanyan, Christoph Schied, Marco Salvi, Aaron Lefohn, Derek Nowrouzezahrai, and Timo Aila. 2017. Interactive Reconstruction of Monte Carlo Image Sequences Using a Recurrent Denoising Autoencoder. *ACM Trans. Graph.* 36, 4, Article Article 98 (2017).
- Jianghao Chang, Benoufinedt Alain, and Victor Ostromoukhov. 2009. Structure-Aware Error Diffusion. *ACM Trans. Graph.* 28, 5 (Dec. 2009), 1–8. <https://doi.org/10.1145/1618452.1618508>
- R. L. Cook. 1986. Stochastic Sampling in Computer Graphics. *ACM Transactions on Graphics* 5, 1 (1986), 51–72.
- Simona Daly. 1987. Subroutine for the generation of a two dimensional human visual contrast sensitivity function.
- S. Daly. 1993. The Visible Differences Predictor: An algorithm for the assessment of image fidelity. In *Digital Image and Human Vision*, A.B. Watson (Ed.). Cambridge,

- MA: MIT Press, 179–206.
- R.J. Deeley, N. Drasdo, and W. N. Charman. 1991. A simple parametric model of the human ocular modulation transfer function. *Ophthalmology and Physiological Optics* 11 (1991), 91–93.
- Mark A. Z. Dippé and Erling Henry Wold. 1985. Antialiasing through stochastic sampling. In *SIGGRAPH '85*.
- James A. Ferwerda, Sumanta N. Pattanaik, Peter Shirley, and Donald P. Greenberg. 1996. A Model of Visual Adaptation for Realistic Image Synthesis. In *Proceedings of the 23rd Annual Conference on Computer Graphics and Interactive Techniques (SIGGRAPH '96)*. Association for Computing Machinery, New York, NY, USA, 249–258. <https://doi.org/10.1145/237170.237262>
- Robert W. Floyd and Louis Steinberg. 1976. An Adaptive Algorithm for Spatial Greyscale. *Proceedings of the Society for Information Display* 17, 2 (1976), 75–77.
- Iliyan Georgiev and Marcos Fajardo. 2016. Blue-noise Dithered Sampling. In *ACM SIGGRAPH 2016 Talks (Anaheim, California) (SIGGRAPH '16)*. ACM, New York, NY, USA, Article 35, 1 pages. <https://doi.org/10.1145/2897839.2927430>
- P. Glasserman. 2004. *Monte Carlo Methods in Financial Engineering*. Springer.
- Alvaro J. González, Jan Bacca Rodríguez, Gonzalo R. Arce, and Daniel Leo Lau. 2006. Alpha stable human visual system models for digital halftoning. In *Electronic Imaging*.
- J. H. Halton. 1964. Algorithm 247: Radical-inverse Quasi-random Point Sequence. *Commun. ACM* 7, 12 (Dec. 1964), 701–702. <https://doi.org/10.1145/355588.365104>
- Eric Heitz and Laurent Belcour. 2019. Distributing Monte Carlo Errors as a Blue Noise in Screen Space by Permuting Pixel Seeds Between Frames. *Computer Graphics Forum* (2019). <https://doi.org/10.1111/cgf.13778>
- Eric Heitz, Laurent Belcour, Victor Ostromoukhov, David Coeurjolly, and Jean-Claude Iehl. 2019. A Low-Discrepancy Sampler that Distributes Monte Carlo Errors as a Blue Noise in Screen Space. In *SIGGRAPH 19 Talks*. ACM, Los Angeles, United States. <https://hal.archives-ouvertes.fr/hal-02150657>
- Edwin Hewitt and Kenneth A. Ross. 1994. *Abstract Harmonic Analysis: Volume I Structure of Topological Groups Integration Theory Group Representations*. SpringerNewYork.
- Sam Hocevar and Gary Nger. 2008. Reinstating Floyd-Steinberg: Improved Metrics for Quality Assessment of Error Diffusion Algorithms, Vol. 5099. 38–45. https://doi.org/10.1007/978-3-540-69905-7_5
- James T. Kajiya. 1986. The Rendering Equation. In *SIGGRAPH '86*, Vol. 20. 143–150.
- Anton S. Kaplanyan, Anton Sochenov, Thomas Leimkühler, Mikhail Okunev, Todd Goodall, and Gizem Rufo. 2019. DeepFovea: Neural Reconstruction for Foveated Rendering and Video Compression Using Learned Statistics of Natural Videos. *ACM Trans. Graph.* 38, 6, Article Article 212 (2019).
- Alexander Keller. 2013. Quasi-Monte Carlo Image Synthesis in a Nutshell. In *Monte Carlo and Quasi-Monte Carlo Methods 2012*, Josef Dick, Frances Y. Kuo, Gareth W. Peters, and Ian H. Sloan (Eds.). Springer Berlin Heidelberg, 213–249.
- Hiroaki Koge, Yasuaki Ito, and Koji Nakano. 2014. A GPU Implementation of Clipping-Free Halftoning Using the Direct Binary Search. In *Algorithms and Architectures for Parallel Processing*, Xian-he Sun, Wenyu Qu, Ivan Stojmenovic, Wanlei Zhou, Zhiyang Li, Hua Guo, Geyong Min, Tingting Yang, Yulei Wu, and Lei Liu (Eds.). Springer International Publishing, Cham, 57–70.
- Lauwerens Kuipers and Harald Niederreiter. 1974. *Uniform Distribution of Sequences*. Wiley, New York, USA.
- Alexandr Kuznetsov, Nima Khademi Kalantari, and Ravi Ramamoorthi. 2018. Deep Adaptive Sampling for Low Sample Count Rendering. *Computer Graphics Forum* 37, 4 (2018), 35–44.
- Daniel L. Lau and Gonzalo R. Arce. 2007. *Modern Digital Halftoning, Second Edition*. CRC Press, Inc., USA.
- T. Lindeberg. 1990. Scale-space for discrete signals. *IEEE Transactions on Pattern Analysis and Machine Intelligence* 12, 3 (1990), 234–254.
- WW Loh. 1995. *On the method of control variates*. Ph.D. Dissertation. Stanford, CA, USA.
- Guillaume Loubet, Nicolas Holzschuch, and Wenzel Jakob. 2019. Reparameterizing discontinuous integrands for differentiable rendering. *Transactions on Graphics (Proceedings of SIGGRAPH Asia)* 38, 6 (Dec. 2019). <https://doi.org/10.1145/3355089.3356510>
- Jeffrey Lubin. 1995. A Visual Discrimination Model for Imaging System Design and Evaluation. In *Vision Models for Target Detection and Recognition*, Eli Peli (Ed.). World Scientific Publishing Company, Inc., 245–283.
- J. Mannos and D. Sakrison. 1974. The effects of a visual fidelity criterion of the encoding of images. *IEEE Transactions on Information Theory* 20, 4 (1974), 525–536. <https://doi.org/10.1109/TIT.1974.1055250>
- Rafal Mantiuk, Scott J. Daly, Karol Myszkowski, and Hans-Peter Seidel. 2005. Predicting visible differences in high dynamic range images: model and its calibration. In *Human Vision and Electronic Imaging X*, Vol. 5666. SPIE, 204–214.
- Rafal Mantiuk, Kiljoong Kim, Allan G. Rempel, and Wolfgang Heidrich. 2011. HDR-VDP-2: a calibrated visual metric for visibility and quality predictions in all luminance conditions. *ACM Transactions on Graphics (Proc. SIGGRAPH)* 30, 4 (2011).
- Panagiotis Takis Metaxas. 2003. Parallel Digital Halftoning by Error-Diffusion. In *Proceedings of the Paris C. Kanellakis Memorial Workshop on Principles of Computing & Knowledge: Paris C. Kanellakis Memorial Workshop on the Occasion of His 50th Birthday* (San Diego, California, USA) (PCK50). Association for Computing Machinery, New York, NY, USA, 35–41. <https://doi.org/10.1145/778348.778355>
- Don P. Mitchell. 1991. Spectrally Optimal Sampling for Distribution Ray Tracing. *SIGGRAPH Comput. Graph.* 25, 4 (July 1991), 157–164. <https://doi.org/10.1145/127719.122736>
- T. Mitsa and K. J. Parker. 1991. Digital halftoning using a blue noise mask. In *Proceedings of International Conference on Acoustics, Speech, and Signal Processing*. 2809–2812 vol.4. <https://doi.org/10.1109/ICASSP.1991.150986>
- K.T. Mullen. 1985. The contrast sensitivity of human colour vision to red-green and blue-yellow chromatic gratings. *Journal of Physiology* 359 (1985), 381–400.
- Karol Myszkowski. 1998. The Visible Differences Predictor: applications to global illumination problems. In *Rendering Techniques '98*, George Drettakis and Nelson Max (Eds.). Springer Vienna, Vienna, 223–236.
- R. Näsänen. 1984. Visibility of halftone dot textures. *IEEE Transactions on Systems, Man, and Cybernetics SMC-14*, 6 (1984), 920–924.
- Harald Niederreiter. 1992. *Random Number Generation and quasi-Monte Carlo Methods*. Society for Industrial and Applied Mathematics, Philadelphia, PA, USA.
- Victor Ostromoukhov. 2001. A Simple and Efficient Error-Diffusion Algorithm. In *Proceedings of the 28th Annual Conference on Computer Graphics and Interactive Techniques (SIGGRAPH '01)*. Association for Computing Machinery, New York, NY, USA, 567–572. <https://doi.org/10.1145/383259.383326>
- Wai-Man Pang, Yingge Qu, Tien-Tsin Wong, Daniel Cohen-Or, and Pheng-Ann Heng. 2008. Structure-Aware Halftoning. In *ACM SIGGRAPH 2008 Papers* (Los Angeles, California) (SIGGRAPH '08). Association for Computing Machinery, New York, NY, USA, Article Article 89, 8 pages. <https://doi.org/10.1145/1399504.1360688>
- Athanasios Papoulis and S. Unnikrishna Pillai. 2002. *Probability, Random Variables, and Stochastic Processes* (fourth ed.). McGraw Hill.
- Thrasylvoulos N. Pappas and David L. Neuhoff. 1999. Least-squares model-based halftoning. *IEEE Transactions on Image Processing* 8, 8 (Aug 1999), 1102–1116. <https://doi.org/10.1109/83.777090>
- Eli Peli, Jian Yang, and Robert B. Goldstein. 1991. Image invariance with changes in size: the role of peripheral contrast thresholds. *J. Opt. Soc. Am. A* 8, 11 (1991), 1762–1774.
- Matt Pharr, Wenzel Jakob, and Greg Humphreys. 2016. *Physically Based Rendering: From Theory To Implementation* (3rd ed.). Morgan Kaufmann Publishers Inc.
- Mahesh Ramasubramanian, Sumanta N. Pattanaik, and Donald P. Greenberg. 1999. A Perceptually Based Physical Error Metric for Realistic Image Synthesis. In *SIGGRAPH '99*. 73–82.
- Ansari Rashid, Guillemot Christine, and Memon Nasir. 2005. 5.5 - Lossy Image Compression: JPEG and JPEG2000 Standards. In *Handbook of Image and Video Processing (Second Edition)*, AL BOVIK (Ed.). Academic Press, 709 – XXII.
- J.G. Robson and Norma Graham. 1981. Probability summation and regional variation in contrast sensitivity across the visual field. *Vision Research* 21, 3 (1981), 409–418.
- Gurprit Singh, Cengiz Oztireli, Abdalla G.M. Ahmed, David Coeurjolly, Kartic Subr, Oliver Deussen, Victor Ostromoukhov, Ravi Ramamoorthi, and Wojciech Jarosz. 2019. Analysis of Sample Correlations for Monte Carlo Rendering. *Comp. Graph Form. (Proc. EGSR)* 38, 2 (2019).
- I. M. Sobol. 1967. The distribution of points in a cube and the approximate evaluation of integrals. *U. S. S. R. Comput. Math. and Math. Phys.* 7 (1967), 86–112. <https://ci.nii.ac.jp/naid/10021313073/en/>
- Givago da Silva Souza, Bruno Duarte Gomes, and Luiz Carlos L. Silveira. 2011. Comparative neurophysiology of spatial luminance contrast sensitivity. *Psychology & Neuroscience* 4 (06 2011), 29 – 48.
- Kevin E. Spaulding, Rodney L. Miller, and Jay S. Schildkraut. 1997. Methods for generating blue-noise dither matrices for digital halftoning. *Journal of Electronic Imaging* 6, 2 (1997), 208 – 230. <https://doi.org/10.1117/12.266861>
- J. Stoffel and J. Moreland. 1981. A Survey of Electronic Techniques for Pictorial Image Reproduction. *IEEE Transactions on Communications* 29, 12 (December 1981), 1898–1925. <https://doi.org/10.1109/TCOM.1981.1094946>
- James R. Sullivan, Lawrence A. Ray, and Rodney Miller. 1991. Design of minimum visual modulation halftone patterns. *IEEE Transactions on Systems, Man, and Cybernetics* 21, 1 (Jan 1991), 33–38. <https://doi.org/10.1109/21.101134>
- R. Ulichney. 1987. *Digital Halftoning*. Cambridge, Massachusetts.
- Robert A. Ulichney. 1993. Void-and-cluster method for dither array generation, Vol. 1913. <https://doi.org/10.1117/12.152707>
- Eric Veach. 1998. *Robust Monte Carlo Methods for Light Transport Simulation*. Ph.D. Dissertation. Stanford, CA, USA. Advisor(s) Guibas, Leonidas J. AAI9837162.
- Valdimir Volevich, Karol Myszkowski, Andrei Khoduev, and Edward A. Kopylov. 2000. Using the Visible Differences Predictor to Improve Performance of Progressive Global Illumination Computation. *ACM Trans. Graph.* 19, 2 (April 2000), 122–161.
- G. Westheimer. 1986. The eye as an optical instrument. In *Handbook of Perception and Human Performance: 1. Sensory Processes and Perception*, K.R. Boff, L. Kaufman, and J.P. Thomas (Eds.). Wiley, New York, 4.1–4.20.

- Sophie Wuerger, Maliha Ashraf, Minjung Kim, Jasna Martinovic, Maria Pérez-Ortiz, and Rafał K. Mantiuk. 2020. Spatio-chromatic contrast sensitivity under mesopic and photopic light levels. *Journal of Vision* 20, 4 (04 2020), 23–23.
- Ji Yellott. 1983. Spectral consequences of photoreceptor sampling in the rhesus retina. *Science* 221, 4608 (1983), 382–385.
- Cheng Zhang, Bailey Miller, Kai Yan, Ioannis Gkioulekas, and Shuang Zhao. 2020. Path-Space Differentiable Rendering. *ACM Trans. Graph.* 39, 6 (2020), 143:1–143:19.
- X. Zhang and B. A. Wandell. 1997. A spatial extension of CIELAB for digital color-image reproduction. *Journal of the Society for Information Display* 5, 1 (1997), 61–63.
- M. Zwicker, W. Jarosz, J. Lehtinen, B. Moon, R. Ramamoorthi, F. Rousselle, P. Sen, C. Soler, and S.-E. Yoon. 2015. Recent Advances in Adaptive Sampling and Reconstruction for Monte Carlo Rendering. *Computer Graphics Forum* 34, 2 (2015), 667–681.

A ERROR DECOMPOSITION

For pixels solving similar light transport integrals, swapping their samples gives a similar result to swapping their estimates: $\mathbf{Q}(\pi(\mathbf{S})) = \pi(\mathbf{Q}(\mathbf{S})) + \mathbf{\Delta}$. The error $\mathbf{\Delta}$ is zero when the swapped pixels solve the same integral. Substituting into Eq. (9), we can bound the perceptual error using the triangle inequality, the discrete Young convolution inequality [Hewitt and Ross 1994], and the Cauchy–Schwarz inequality:

$$E(\pi(\mathbf{S})) = \|\mathbf{g} * (\pi(\mathbf{Q}(\mathbf{S})) - \mathbf{I} + \mathbf{\Delta})\|_2^2 \quad (14a)$$

$$= \|\mathbf{g} * (\pi(\mathbf{Q}(\mathbf{S})) - \mathbf{I})\|_2^2 + \|\mathbf{g} * \mathbf{\Delta}\|_2^2 + 2\langle \mathbf{g} * (\pi(\mathbf{Q}(\mathbf{S})) - \mathbf{I}), \mathbf{g} * \mathbf{\Delta} \rangle \quad (14b)$$

$$\leq \|\mathbf{g} * (\pi(\mathbf{Q}(\mathbf{S})) - \mathbf{I})\|_2^2 + \|\mathbf{g}\|_1^2 \|\mathbf{\Delta}\|_2^2 + 2\|\mathbf{g}\|_1^2 \|\pi(\mathbf{Q}(\mathbf{S})) - \mathbf{I}\|_2 \|\mathbf{\Delta}\|_2. \quad (14c)$$

The first summand in Eq. (14b) involves pixel permutations in the readily available estimated image $\mathbf{Q}(\mathbf{S})$. In the second and third summands we ideally want to use an approximation for the terms involving $\mathbf{\Delta}$ that forgoes rendering invocations:

$$E(\pi(\mathbf{S})) \approx \|\mathbf{g} * (\pi(\mathbf{Q}(\mathbf{S})) - \mathbf{I})\|_2^2 + \|\mathbf{g}\|_1^2 \sum_i d(i, \pi(i)) = E_{\mathbf{\Delta}}(\pi, \mathbf{S}). \quad (15)$$

We approximate the terms involving $\|\mathbf{\Delta}\|_2$ with a *dissimilarity metric* $d(i, j)$ between any two pixels i and j . The purpose of this metric is to predict how different we expect the result of swapping the sample sets of i and j to be, compared to only swapping their pixel values Q_i and Q_j . It can be constructed based on assumptions or prior knowledge about the image coming from, e. g., auxiliary buffers (depth, normals, etc).

In our implementation we use a simple binary dissimilarity function returning zero when i and j are within distance r and infinity otherwise;³ we set r between 1 and 3. This allows us to restrict the search space $\Pi(\mathbf{S})$ only to permutations that swap adjacent pixels such that it is more likely that $\mathbf{\Delta}$ is small. More elaborate heuristics can be devised in the future to better account for pixel (dis)similarity.

B HANDLING BIAS TOWARDS SURROGATE

The trade-off between white noise and bias towards a surrogate can be controlled by modifying the original energy to also include a data term that penalizes large deviations from the initial unbiased white noise image $\mathbf{Q}(\mathbf{S})$ (for a derivation see Section 3 in the

³The radius should ideally depend on the image smoothness/regularity, and can be locally adapted.

supplemental):

$$\sqrt{E_c(\mathbf{S}')} = c \|\mathbf{g}\|_1 \|\mathbf{Q}(\mathbf{S}') - \mathbf{Q}(\mathbf{S})\|_2 \quad (16)$$

$$+ (1 - c) \|\mathbf{g} * \mathbf{Q}(\mathbf{S}') - \mathbf{h} * \mathbf{I}'\|_2. \quad (17)$$

Our original formulation is retrieved for $c = 0$, while the initial image is enforced for $c = 1$, and the parameter can be varied in $[0, 1]$ to achieve different levels of bias. The parameter $1 - c$ is a smoothness/bias parameter describing how much one trusts the surrogate (or equivalently the quality of the surrogate). For greater control c may be defined per-pixel, in which case it can be multiplied componentwise with the vector inside the norm $\|\cdot\|_2$.

Table 2. MSE and pMSE metrics for various methods on different scenes rendered at 4 samples per pixel. All methods aim to minimize the pMSE. We note that our methods consistently outperform current state of the art [Heitz and Belcour 2019]. Notably, every method is superior to the histogram sampling approach, and all of our methods except for dithering are better than the permutation approach. The occasional better performance of *horizontal* methods can be explained by the fact that they always choose from 4spp estimates, while *vertical* methods choose from 1spp estimates (except for 2^N which uses estimates with 1-4spp). The scene for *horizontal* approaches is kept static and the metrics for the 16th frame are presented. Thus this is the ideal scenario for such methods, so metrics there may even have an unfair advantage over *vertical* ones, since generally the scene cannot be assumed to be static in an animation sequence.

Method	Bathroom		Classroom		Grey Room		Living Room		Modern Hall		San Miguel		Staircase		White Room	
	MSE $\times 10^{-2}$	pMSE $\times 10^{-3}$	MSE $\times 10^{-2}$	pMSE $\times 10^{-3}$	MSE $\times 10^{-2}$	pMSE $\times 10^{-2}$	MSE $\times 10^{-2}$	pMSE $\times 10^{-3}$	MSE $\times 10^{-2}$	pMSE $\times 10^{-2}$	MSE $\times 10^{-2}$	pMSE $\times 10^{-3}$	MSE $\times 10^{-3}$	pMSE $\times 10^{-3}$	MSE $\times 10^{-2}$	pMSE $\times 10^{-3}$
nonoptimized 1 spp	3.58	8.19	7.13	16.03	11.45	6.81	5.76	12.91	11.44	4.09	6.85	18.93	18.82	7.79	5.75	18.23
nonoptimized 4 spp	1.40	3.15	3.13	7.91	7.91	3.02	3.37	5.61	5.22	1.70	3.58	8.92	8.88	5.60	2.78	7.98
Dither (Ours)	1.31	3.31	4.36	11.63	8.46	5.07	2.27	4.43	5.25	1.80	3.74	11.19	7.80	5.36	2.51	7.95
Error diffusion (Ours)	1.22	2.27	4.91	7.03	8.76	2.82	2.08	2.31	4.86	1.33	5.07	8.50	6.87	5.08	2.19	5.16
Iterative <i>vertical</i> (Ours)	2.32	2.02	6.00	6.10	9.07	2.97	4.32	1.86	7.15	1.29	5.51	7.05	10.50	4.45	3.98	5.00
Iterative <i>vertical</i> 2^N (Ours)	1.26	1.66	3.12	4.91	7.53	2.82	2.46	1.13	4.55	1.18	3.31	5.85	7.08	4.31	2.26	4.58
Histogram [2019]	3.58	6.29	7.11	13.08	11.49	6.67	5.75	9.88	11.43	3.60	6.84	16.52	18.90	6.69	5.75	14.09
Relocation (Ours, frame 16)	1.52	2.06	3.83	5.31	8.34	2.41	3.59	1.59	5.46	1.18	3.94	7.31	7.67	4.30	2.93	4.72
Permutation [2019] (frame 16)	1.40	2.79	3.15	7.25	7.90	2.84	3.38	3.14	5.21	1.51	3.59	8.51	8.87	5.40	2.72	6.73

Table 3. Timings for the minimization of the energy for various methods on different scenes rendered at 4 samples per pixel. Note that the timings do not include the construction of the surrogate. We see that our error diffusion approach is consistently the fastest method, since it doesn't require any sorting. Our dithering approach is comparable to Heitz and Belcour's approaches in terms of speed, since those use a similar minimization strategy relying on sorting. Finally, our iterative minimization methods are the slowest. We note that those were not optimized, and based on [Analoui and Allebach 1992; Koge et al. 2014] a speed-up of 300 \times can be expected (for larger kernels and images the speed-up can be even larger). Additional optimization strategies are discussed in the supplemental.

Method	Bathroom	Classroom	Grey Room	Living Room	Modern Hall	San Miguel	Staircase	White Room
Dither (Ours)	0.07	0.08	0.07	0.07	0.02	0.12	0.09	0.07
Error diffusion (Ours)	0.04	0.03	0.04	0.04	0.01	0.06	0.04	0.04
Iterative <i>vertical</i> (Ours)	18.44	111.41	12.82	15.26	5.43	29.09	15.21	19.45
iterative <i>vertical</i> 2^N (Ours)	95.09	404.12	59.69	83.41	23.93	137.89	35.39	102.05
Histogram [2019]	0.06	0.07	0.11	0.06	0.02	0.09	0.08	0.06
Relocation (Ours, frame 16)	23.04	21.57	22.00	30.08	8.48	36.36	23.78	22.76
Permutation [2019] (frame 16)	0.10	0.10	0.10	0.11	0.03	0.21	0.10	0.14

Table 4. MSE and pMSE metrics for various methods on different scenes rendered at 16 samples per pixel. All methods aim to minimize the pMSE. We note that our methods consistently outperform current state of the art [Heitz and Belcour 2019]. Notably, every method is superior to the histogram sampling approach.

Method	Bathroom		Classroom		Grey Room		Living Room		Modern Hall		San Miguel		Staircase		White Room	
	MSE $\times 10^{-3}$	pMSE $\times 10^{-3}$	MSE $\times 10^{-2}$	pMSE $\times 10^{-3}$	MSE $\times 10^{-2}$	pMSE $\times 10^{-2}$	MSE $\times 10^{-2}$	pMSE $\times 10^{-3}$	MSE $\times 10^{-2}$	pMSE $\times 10^{-3}$	MSE $\times 10^{-2}$	pMSE $\times 10^{-3}$	MSE $\times 10^{-3}$	pMSE $\times 10^{-3}$	MSE $\times 10^{-2}$	pMSE $\times 10^{-3}$
nonoptimized 4 spp	14.03	3.13	3.15	7.92	7.88	3.02	3.38	5.62	5.24	17.06	3.53	8.73	7.18	4.53	2.78	7.96
nonoptimized 16 spp	4.94	1.47	1.55	4.89	3.77	1.04	1.23	2.18	2.14	8.02	1.10	4.67	3.39	3.78	1.35	3.62
Dither (Ours)	4.97	1.52	1.15	4.69	4.12	1.36	1.09	1.82	1.93	8.30	1.49	5.38	3.09	3.73	0.91	2.98
Error diffusion (Ours)	4.07	1.20	0.94	3.85	4.00	0.87	0.86	1.07	1.68	6.57	1.33	4.70	2.76	3.69	0.73	2.13
Iterative <i>vertical</i> (Ours)	9.03	1.10	2.03	3.35	5.17	0.84	2.30	0.84	3.03	6.39	2.39	4.02	4.46	3.14	1.75	1.99
Histogram [2019]	13.98	2.37	3.12	6.20	7.88	2.72	3.36	3.57	5.23	14.78	3.52	6.82	7.13	4.09	2.77	5.77

Perceptual Error Optimization for Monte Carlo Rendering:

Supplemental document

VASSILLEN CHIZHOV, MIA Group Saarland University, Max-Planck-Institut für Informatik, Germany
 ILIYAN GEORGIEV, Autodesk, United Kingdom
 KAROL MYSZKOWSKI, Max-Planck-Institut für Informatik, Germany
 GURPRIT SINGH, Max-Planck-Institut für Informatik, Germany

Additional Key Words and Phrases: path tracing, perceptual error, blue noise, sampling

1 OVERVIEW

In the current supplemental we discuss various details related to our general formulation from the main paper. We start with a description of the extension of our framework to the *a-priori* setting (Section 2). Then we show how the reference image substitution with a surrogate can be translated to a more general problem (Section 3), which also allows optimizing how close the result fits to the surrogate. In Section 4 we describe a way in which textures can be accounted for in our *horizontal* approach, so that mispredictions due to multiplicative (and additive) factors are eliminated. In Section 5 we describe ways in which the runtime of iterative energy minimization methods can be improved considerably. Notably, an expression is derived allowing the energy difference due to trial swaps to be evaluated in constant time (no scaling with image size or kernel size). In the remaining sections we analyze how current *a-posteriori* [Heitz and Belcour 2019] and *a-priori* [Georgiev and Fajardo 2016; Heitz et al. 2019] state of the art approaches can be related to our framework. Interpretations are discussed, major sources of error are identified, and the assumptions of the algorithms are made explicit.

2 OUR A-PRIORI APPROACH

We extend our theory to the *a-priori* setting and discuss the main factors affecting the quality. The quality of *a-priori* approaches is determined mainly by three factors: the energy, the search space, and the optimization strategy. We discuss each of those briefly in the following paragraphs.

Our energy. We extend the *a-posteriori* energy from the main paper in order to handle multiple estimators involving different integrands: $\mathbf{Q}_1, \dots, \mathbf{Q}_T$, with associated weights w_1, \dots, w_T :

$$E(\mathbf{S}) = \sum_{t=1}^T w_t \|\mathbf{g} * \mathbf{Q}_t(\mathbf{S}) - \mathbf{I}_t\|^2. \quad (1)$$

In the above \mathbf{g} would typically be a low-pass kernel (e. g., Gaussian), and \mathbf{I}_t is the integral of the function used in the estimator \mathbf{Q}_t . Through this energy a whole set of functions can be optimized for, in order for the sequence to be more robust to different scenes and estimators, that do not fit any of the considered integrands exactly.

Authors' addresses: Vassillen Chizhov, MIA Group Saarland University, Max-Planck-Institut für Informatik, Saarbrücken, Germany; Iliyan Georgiev, Autodesk, United Kingdom; Karol Myszkowski, Max-Planck-Institut für Informatik, Saarbrücken, Germany; Gurprit Singh, Max-Planck-Institut für Informatik, Saarbrücken, Germany.

We note that the derived optimization in Section 5 is also applicable to the minimization of the proposed energy.

Search space. The search space plays an important role towards the qualities which the optimized sequences exhibit. A more restricted search space provides more robustness and may help avoid overfitting to the considered set of integrands.

For instance, sample sets may be generated randomly within each pixel. Then, their assignment to pixels may be optimized over the space of all possible permutations. This is the setting of *horizontal* methods. If additionally this assignment is done within each dimension separately it allows for an even better fit to the integrands in the energy. The scrambling keys' search space in [Heitz et al. 2019] is a special case of the latter applied for the Sobol sequence.

Constraining the search space to points generated from low-discrepancy sequences provides further robustness and guarantees desirable integration properties of the considered sequences. Similarly to [Heitz et al. 2019], we can consider a search space of Sobol scrambling keys in order for the optimized sequence to have a low discrepancy.

Ideally, such integration properties should arise directly from the energy. However, in practice the scene integrand cannot be expected to exactly match the set of considered integrands, thus extra robustness is gained through the restriction. Additionally, optimizing for many dimensions at the same time is costly as noted in [Heitz et al. 2019], thus imposing low-discrepancy properties also helps in that regard.

Finally, by imposing strict search space constraints a severe restriction on the distribution of the error is imposed. This can be alleviated by imposing the restrictions through soft penalty terms in the energy. This can allow for a trade-off between blue noise distribution and integration quality for example.

Progressive rendering. In order to make the sequence applicable in progressive rendering, subsets of samples should be considered in the optimization. Given a sample set S_i for pixel i we can decompose it in sample sets of $1, \dots, N$ samples: $S_{i,1} \subset \dots \subset S_{i,N} \equiv S_i$. We denote the respective images of sample sets $\mathbf{S}_1, \dots, \mathbf{S}_N$.

Then an energy that also optimizes for the distribution of the error at each sample count is:

$$E(\mathbf{S}) = \sum_{t=1}^T \sum_{k=1}^N w_{t,k} \|\mathbf{g} * \mathbf{Q}_t(\mathbf{S}_k) - \mathbf{I}_t\|^2. \quad (2)$$

If $w_{i,k}$ are set to zero for $k < N$ then the original formulation is recovered. The more general formulation imposes additional constraints on the samples, thus the quality at the full sample count

may be compromised if we also require a good quality at lower sample counts.

Choosing samples from S_i for $S_{i,1}, \dots, S_{i,N-1}$ (in each dimension) constitutes a *vertical* search space analogous to the one discussed in the main paper for *a-posteriori* methods. The ranking keys' optimisation in [Heitz et al. 2019] is a special case of this search space for the Sobol sequence.

Adaptive sampling can be handled by allowing a varying number of samples per pixel, and a corresponding energy derived from the one above. Note that this poses further restrictions on the achievable distribution.

Optimization strategies. Typically the energies for *a-priori* methods have been optimized through simulated annealing [Georgiev and Fajardo 2016; Heitz et al. 2019]. Metaheuristics can lead to very good minima especially if the runtime is not of great concern, which is the case since the sequences are precomputed. Nevertheless, the computation still needs to be tractable. The energies in previous works are generally not cheap to evaluate. On the other hand, our energies, especially if the optimizations in Section 5 are considered, can be evaluated very efficiently. This is beneficial for keeping the runtime of metaheuristics manageable, allowing for more complex search spaces to be considered.

Implementation details. Implementation decisions for a renderer, such as how samples are consumed, or how those are mapped to the hemisphere and light sources affect the estimator \mathbf{Q} . This is important, especially when choosing \mathbf{Q} for the described energies to optimize a sequence. It is possible that very small implementation changes make a previously ideal sequence useless for a specific renderer. It is important to keep this in mind when optimising sequences by using the proposed energies and when those are used in a renderer.

3 SURROGATE SUBSTITUTION

For practical algorithms we substitute the reference image \mathbf{I} with a surrogate \mathbf{I}' . It is instructive to consider error bounds in relation to that, and subsequently extend the formulation to one that allows control over the amount of bias towards the surrogate. We denote $\mathbf{Q}_0 = \mathbf{Q}(\mathbf{S})$, and $\mathbf{Q}' = \mathbf{Q}(\mathbf{S}')$, where we want to optimize for the latter, and \mathbf{Q}_0 remains fixed.

$$\begin{aligned} & \|\mathbf{g} * \mathbf{Q}' - \mathbf{h} * \mathbf{I}\|_2 = \\ & \|\mathbf{g} * \mathbf{Q}' - \mathbf{h} * \mathbf{I}' + \mathbf{h} * (\mathbf{I}' - \mathbf{I})\|_2 \leq \\ & \|\mathbf{g} * \mathbf{Q}' - \mathbf{h} * \mathbf{I}'\|_2 + \|\mathbf{h} * (\mathbf{I}' - \mathbf{I})\|_2 \end{aligned} \quad (3)$$

The above bound results in the original formulation when considering only the first term. We can also bound the error through a term involving \mathbf{Q}_0 :

$$\begin{aligned} & \|\mathbf{g} * \mathbf{Q}' - \mathbf{h} * \mathbf{I}\|_2 = \\ & \|\mathbf{g} * (\mathbf{Q}' - \mathbf{Q}_0) + (\mathbf{g} * \mathbf{Q}_0 - \mathbf{h} * \mathbf{I})\|_2 \leq \\ & \|\mathbf{g}\|_1 \|\mathbf{Q}' - \mathbf{Q}_0\|_2 + \|\mathbf{g} * \mathbf{Q}_0 - \mathbf{h} * \mathbf{I}\|_2. \end{aligned} \quad (4)$$

Combining the two with weights c and $(1 - c)$, for $c \in [0, 1]$ yields:

$$\begin{aligned} & \|\mathbf{g} * \mathbf{Q}' - \mathbf{h} * \mathbf{I}\|_2 \leq \\ & c \|\mathbf{g}\|_1 \|\mathbf{Q}' - \mathbf{Q}_0\|_2 + (1 - c) \|\mathbf{g} * \mathbf{Q}' - \mathbf{h} * \mathbf{I}'\|_2 + \\ & c \|\mathbf{g} * \mathbf{Q}_0 - \mathbf{h} * \mathbf{I}\|_2 + (1 - c) \|\mathbf{h} * (\mathbf{I}' - \mathbf{I})\|_2. \end{aligned} \quad (5)$$

We assume $\mathbf{g}, \mathbf{h}, \mathbf{I}, \mathbf{I}', \mathbf{Q}_0$, and c to be fixed, and our optimization variable to be \mathbf{Q}' . Then the optimization problem simplifies to:

$$\min_{\mathbf{Q}'} c \|\mathbf{g}\|_1 \|\mathbf{Q}' - \mathbf{Q}_0\|_2 + (1 - c) \|\mathbf{g} * \mathbf{Q}' - \mathbf{h} * \mathbf{I}'\|_2 \quad (6)$$

The standard energy that we use is retrieved for $c = 0$ in which case:

$$\arg \min_{\mathbf{Q}'} \|\mathbf{g} * \mathbf{Q}' - \mathbf{h} * \mathbf{I}'\|_2 = \arg \min_{\mathbf{Q}'} \|\mathbf{g} * \mathbf{Q}' - \mathbf{h} * \mathbf{I}'\|_2^2. \quad (7)$$

4 TEXTURE DEMODULATION FOR OUR HORIZONTAL APPROACH

Our iterative energy minimization algorithms (Alg. 1, Alg. 2) directly work with the original energy formulation, unlike error diffusion and dither matrix halftoning which only approximately minimize our energy. This allows textures to be handled more robustly compared to the permutation approach of Heitz and Belcour.

Reducing misprediction errors. Our *horizontal* approach relies on a dissimilarity metric $d(\cdot, \cdot)$ which approximates terms involving the difference Δ due to swapping sample sets instead of pixels. This difference can be decreased, so that d is a better approximation, if additional information is factored out in the energy: screen-space varying multiplicative and additive terms. Specifically, if we have a spatially varying multiplicative image α , and a spatially varying additive image β :

$$\mathbf{Q} = \alpha \mathbf{Q}' + \beta \quad (8)$$

$$\Delta'(\pi) = \alpha \odot \mathbf{Q}'(\pi(\mathbf{S})) - \alpha \odot \pi(\mathbf{Q}'(\mathbf{S})) \quad (9)$$

$$\Delta(\pi) = \mathbf{Q}(\pi(\mathbf{S})) - \pi(\mathbf{Q}(\mathbf{S})) = \quad (10)$$

$$\alpha \odot \mathbf{Q}'(\pi(\mathbf{S})) + \beta - \pi(\alpha \odot \mathbf{Q}'(\mathbf{S}) + \beta),$$

we can make use of this in our formulation:

$$E(\pi) = \|\mathbf{g} * \mathbf{Q}(\pi(\mathbf{S})) - \mathbf{h} * \mathbf{I}\|_2^2 \quad (11)$$

$$\sqrt{E(\pi)} \leq \|\mathbf{g} * (\alpha \odot \pi(\mathbf{Q}'(\mathbf{S})) + \beta) - \mathbf{h} * \mathbf{I}\|_2 + \|\mathbf{g}\|_1 \|\Delta'\|_2. \quad (12)$$

Contrast this to the original formulation where α and β are not factored out:

$$\sqrt{E(\pi)} \leq \|\mathbf{g} * \pi(\alpha \odot \mathbf{Q}'(\mathbf{S}) + \beta) - \mathbf{h} * \mathbf{I}\|_2 + \|\mathbf{g}\|_1 \|\Delta\|_2. \quad (13)$$

With the new formulation it is sufficient that $\mathbf{Q}'(\pi(\mathbf{S})) = \pi(\mathbf{Q}'(\mathbf{S}))$ for Δ' to be zero, while originally both α and β play a role in Δ becoming zero. Intuitively this means that screen space integrand differences due to additive and multiplicative factors do not result in mispredictions with the new formulation, if the integrand is assume to be the same (locally) in screen space.

Comparison to demodulation. In the method of Heitz and Belcour the permutation is applied on the albedo demodulated image. This preserves the property that the global minimum of the implicit energy can be found through sorting. Translated to our framework

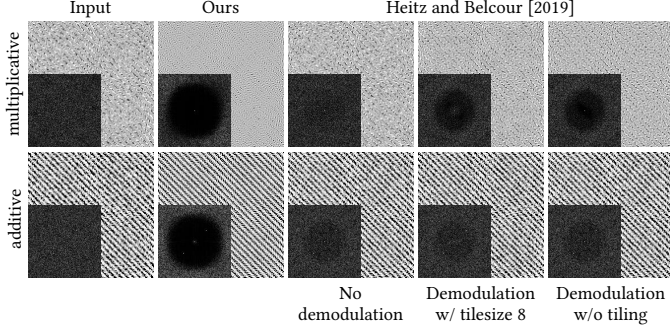


Fig. 1. We demonstrate the importance of the extension presented in Section 4. A high-frequency sinusoidal texture is corrupted by white noise (leftmost column) multiplicatively (**top row**) and additively (**bottom row**). Contrary to Heitz and Belcour’s method, our optimization distributes error as a high-quality blue-noise distribution (see the power-spectrum insets). The reference images for the top/bottom image are respectively a flat grey and a sinusoidal image.

this can be formulated as (\mathbf{B} is a blue noise mask optimized for a kernel \mathbf{g}):

$$E_{HBP}(\pi) = \|\pi(\mathbf{Q}'(\mathbf{S})) - \mathbf{I}' - \mathbf{B}\|_2^2 \approx \|\mathbf{g} * \pi(\mathbf{Q}'(\mathbf{S})) - \mathbf{g} * \mathbf{I}'\|_2^2. \quad (14)$$

We have assumed that β is zero, but we can also extend the method to handle an additive term β as in our case. The more important distinction is that while the albedo demodulated image \mathbf{Q}' is used in the permutation, it is never remodulated ($\alpha \odot \cdot$ is missing). Thus, this does not allow for proper handling of textures, even if it allows for modest improvements in practice. An example of a fail case consists of an image α that is close to white noise. Then the error distribution will also be close to white noise due to the missing $\alpha \odot \cdot$ factor. More precisely, even if $\pi(\mathbf{Q}'(\mathbf{S})) - \mathbf{I}'$ is distributed as \mathbf{B} , this does not imply that $\alpha \odot \pi(\mathbf{Q}'(\mathbf{S})) - \mathbf{I}'$ will be distributed similarly. Dropping $\alpha \odot \cdot$ is, however, a reasonable option if one is restricted to sorting as an optimisation strategy.

We propose a modification of the original approach (and energy) such that not only the demodulated estimator values are used, but the blue noise mask \mathbf{B} is also demodulated. To better understand how it is derived (and how β may be integrated) we study a bound based on the assumption that $\alpha_i \in [0, 1]$, and $\Delta' = 0$

$$E(\pi) = \|\mathbf{g} * (\alpha \odot \pi(\mathbf{Q}'(\mathbf{S})) + \beta) - \mathbf{g} * \mathbf{I}'\|_2^2 \approx \quad (15)$$

$$\|\alpha \odot \pi(\mathbf{Q}'(\mathbf{S})) + \beta - \mathbf{I}' - \mathbf{B}\|_2^2 = \quad (16)$$

$$\sum_i \alpha_i^2 \left((\pi(\mathbf{Q}'(\mathbf{S})))_i + \frac{\beta_i - \mathbf{I}'_i - \mathbf{B}_i}{\alpha_i} \right)^2 \leq \quad (17)$$

$$\|\pi(\mathbf{Q}'(\mathbf{S})) + \frac{\beta - \mathbf{I}' - \mathbf{B}}{\alpha}\|_2^2. \quad (18)$$

The global minimum of the last energy (w.r.t. π) can be found through sorting also, since there is no spatially varying multiplicative factor α in front of the permutation.

Sinusoidal Textures. To demonstrate texture handling (multiplicative term α), in the top row of Fig. 1, a white-noise texture W is multiplied to a sine-wave input signal: $f(x, y) = 0.5 * (1.0 + \sin(x + y)) * W(x, y)$. The reference is a constant image at 0.5. Heitz and Belcour

proposed to handle such textures by applying their method on the albedo-demodulated image. While this strategy may lead to a modest improvement, it ignores the fact that the image is produced by remodulating the albedo, which can negate that improvement. Instead, our *horizontal* iterative minimization algorithm can incorporate the albedo explicitly using the discussed energy.

The bottom row demonstrates the effect of a non-flat signal on the error distribution (additive term β). Here W is added to a sine-wave input signal: $f(x, y) = 0.5 * (1.0 + \sin(x + y)) + W(x, y)$. The reference image is $0.5 * (1 + \sin(x + y))$. Our optimization is closer to the reference suggesting that our method can greatly outperform the current state of the art by properly accounting for auxiliary information, especially in regions with high-frequency textures.

Dimensional decomposition. The additive factor β can be used to motivate splitting the optimization over several dimensions, since the Liouville–Neumann expansion of the rendering equation is additive [Kajiya 1986]. If some dimensions are smooth (e. g., lower dimensions), then a screen space local integrand similarity assumption can be encoded in $d(\cdot, \cdot)$ and it will approximate Δ better for smoother dimensions. If the optimization is applied over all dimensions at the same time, this may result in many mispredictions due to the assumption being violated for dimensions in which the integrand is less smooth in screen space (e. g., higher dimensions). We propose splitting the optimization problem starting from lower dimensions and sequentially optimizing higher dimensions while encoding a local smoothness (in screen space) assumption on the integrand in $d(\cdot, \cdot)$ (e. g., swaps limited to a small neighbourhood around the pixel). This requires solving several optimization problems, but potentially reduces the amount of mispredictions. Note that it does not require more rendering operations than usual.

5 ITERATIVE METHODS OPTIMIZATION

The main cost of iterative minimization methods is computing the energy for each trial swap, more specifically the required convolution and the subsequent norm computation. In the work of Analoui and Allebach an optimisation has been proposed to efficiently evaluate such trial swaps, without recomputing a convolution or norm at each step, yielding a speed up of more than 10 times. The optimisation relies on the assumption that the kernel \mathbf{g} is the same in screen space (the above optimization is not applicable for spatially varying kernels). We extend the described optimisation to a more general case, also including spatially varying kernels. We also note some details not mentioned in the original paper.

5.1 Horizontal swaps

We will assume the most general case: instead of just swapping pixels, we consider swapping sample sets from which values are generated through \mathbf{Q} . It subsumes both swapping pixel values and swapping pixel values in the presence of a multiplicative factor α .

Single swap. The main goal is to evaluate the change of the energy δ due to a swap between the sample sets of some pixels a, b . More precisely, if the original sample set image is \mathbf{S} then the new sample set image is \mathbf{S}' such that $S'_a = S_b, S'_b = S_a$, and $S'_i = S_i$ everywhere else. This corresponds to images: $\mathbf{Q} = \mathbf{Q}(\mathbf{S})$ and $\mathbf{Q}' = \mathbf{Q}(\mathbf{S}')$. The

two images differ only in the pixels with indices a and b . Let:

$$\delta_a = Q'_a - Q_a = Q_a(S_b) - Q_a(S_a) \quad (19)$$

$$\delta_b = Q'_b - Q_b = Q_b(S_a) - Q_b(S_b). \quad (20)$$

We will also denote the convolved images $\tilde{Q} = \mathbf{g} * \mathbf{Q}$ and $\tilde{Q}' = \mathbf{g} * \mathbf{Q}'$, and also $\boldsymbol{\epsilon} = \tilde{Q} - \mathbf{I}$. Specifically:

$$\tilde{Q}_i = \sum_{j \in \mathbb{Z}^2} Q_j g_{i-j}, \quad \tilde{Q}'_i = \tilde{Q}_i + \delta_a g_{i-a} + \delta_b g_{i-b}. \quad (21)$$

We want to be able to efficiently evaluate $\delta = \|\tilde{Q}' - \mathbf{I}\|^2 - \|\tilde{Q} - \mathbf{I}\|^2$, since in the iterative minimization algorithms the candidate with the minimum δ is kept. Using the above expressions for \tilde{Q}'_i we rewrite δ as:

$$\delta = \|\tilde{Q}' - \mathbf{I}\|^2 - \|\tilde{Q} - \mathbf{I}\|^2 = \quad (22)$$

$$\sum_{i \in \mathbb{Z}^2} \|\tilde{Q}_i - I_i + \delta_a g_{i-a} + \delta_b g_{i-b}\|^2 - \|\tilde{Q}_i - I_i\|^2 = \quad (23)$$

$$2 \sum_{i \in \mathbb{Z}^2} \langle \tilde{Q}_i - I_i, \delta_a g_{i-a} + \delta_b g_{i-b} \rangle + \sum_{i \in \mathbb{Z}^2} \|\delta_a g_{i-a} + \delta_b g_{i-b}\|^2 = \quad (24)$$

$$2 \langle \delta_a, \sum_{i \in \mathbb{Z}^2} \epsilon_i g_{i-a} \rangle + 2 \langle \delta_b, \sum_{i \in \mathbb{Z}^2} \epsilon_i g_{i-b} \rangle + \quad (25)$$

$$\langle \delta_a^2, \sum_{i \in \mathbb{Z}^2} g_{i-a} g_{i-a} \rangle + \langle \delta_b^2, \sum_{i \in \mathbb{Z}^2} g_{i-b} g_{i-b} \rangle + \quad (25)$$

$$2 \langle \delta_a \delta_b, \sum_{i \in \mathbb{Z}^2} g_{i-a} g_{i-b} \rangle =$$

$$2 \langle \delta_a, C_{\mathbf{g}, \boldsymbol{\epsilon}}(a) \rangle + 2 \langle \delta_b, C_{\mathbf{g}, \boldsymbol{\epsilon}}(b) \rangle + \quad (26)$$

$$\langle (\delta_a^2 + \delta_b^2), C_{\mathbf{g}, \mathbf{g}}(0) \rangle + 2 \langle \delta_a \delta_b, C_{\mathbf{g}, \mathbf{g}}(b-a) \rangle,$$

where $C_{f,h}(x) = \sum_{i \in \mathbb{Z}^2} f(i-x)h(i)$ is the cross-correlation of f and h . We have reduced the computation of δ to the sum of only 4 terms. Assuming that $C_{\mathbf{g}, \mathbf{g}}$ is known (it can be precomputed once for a known kernel) and that $C_{\mathbf{g}, \boldsymbol{\epsilon}}$ is known (it can be recomputed after a sufficient amount of swaps have been accepted), then evaluating a trial swap takes constant time (it does not scale in the size of the image or the size of the kernel).

Multiple accepted swaps. It may be desirable to avoid recomputing $C_{\mathbf{g}, \boldsymbol{\epsilon}}$ even upon accepting a trial swap. For that purpose we extend the strategy from [Analoui and Allebach 1992] for computing $C_{\mathbf{g}, \boldsymbol{\epsilon}^n}$, where $\boldsymbol{\epsilon}^n$ is the error image after n swaps have been accepted:

$$\{(\delta_{a^1}, \delta_{b^1}), \dots, (\delta_{a^n}, \delta_{b^n})\}. \quad (27)$$

This implies: $\tilde{Q}_i^n = \tilde{Q}_i + \sum_{k=1}^n (\delta_{a^k} g_{i-a^k} + \delta_{b^k} g_{i-b^k})$, and consequently:

$$C_{\mathbf{g}, \boldsymbol{\epsilon}^n}(x) = \quad (28)$$

$$\sum_{i \in \mathbb{Z}^2} \left(\tilde{Q}_i - I_i + \sum_{k=1}^n (\delta_{a^k} g_{i-a^k} + \delta_{b^k} g_{i-b^k}) \right) g_{i-x} = \quad (29)$$

$$C_{\mathbf{g}, \boldsymbol{\epsilon}}(x) + \sum_{k=1}^n (\delta_{a^k} C_{\mathbf{g}, \mathbf{g}}(x-a^k) + \delta_{b^k} C_{\mathbf{g}, \mathbf{g}}(x-b^k)). \quad (30)$$

This allows avoiding the recomputation of $C_{\mathbf{g}, \boldsymbol{\epsilon}}$ after every accepted swap, and instead, the delta on the $n+1$ -st swap with trial differences

δ_a, δ_b is:

$$\delta^{n+1} = \|\mathbf{Q}^{n+1} - \mathbf{I}\|^2 - \|\mathbf{Q}^n - \mathbf{I}\|^2 = \quad (31)$$

$$2 \langle \delta_a, C_{\mathbf{g}, \boldsymbol{\epsilon}^n}(a) \rangle + 2 \langle \delta_b, C_{\mathbf{g}, \boldsymbol{\epsilon}^n}(b) \rangle + \quad (32)$$

$$\langle (\delta_a^2 + \delta_b^2), C_{\mathbf{g}, \mathbf{g}}(0) \rangle + 2 \langle \delta_a \delta_b, C_{\mathbf{g}, \mathbf{g}}(b-a) \rangle,$$

where $C_{\mathbf{g}, \boldsymbol{\epsilon}^n}$ is computed from $C_{\mathbf{g}, \boldsymbol{\epsilon}}$ and $C_{\mathbf{g}, \mathbf{g}}$ as derived in Eq. (22). This computation scales only in the number of accepted swaps since the last recomputation of $C_{\mathbf{g}, \boldsymbol{\epsilon}}$. We also note that $C_{\mathbf{g}, \mathbf{g}}(x-y)$ evaluates to zero if $x-y$ is outside of the support of $C_{\mathbf{g}, \mathbf{g}}$. Additional optimisations have been devised due to this fact [Analoui and Allebach 1992].

5.2 Vertical swaps

In the *vertical* setting swaps happen only within the pixel itself, that is: $\delta_a = Q_a(S'_a) - Q_a(S_a)$. Consequently, $\tilde{Q}'_i = \tilde{Q}_i + \delta_a g_{i-a}$. Computing the difference in the energies for the $n+1$ -st swap:

$$\delta^{n+1} = \|\tilde{Q}^{n+1} - \mathbf{I}\|^2 - \|\tilde{Q}^n - \mathbf{I}\|^2 = \quad (33)$$

$$\sum_{i \in \mathbb{Z}^2} \|\tilde{Q}_i^n - I_i + \delta_a g_{i-a}\|^2 - \|\tilde{Q}_i^n - I_i\|^2 = \quad (34)$$

$$2 \sum_{i \in \mathbb{Z}^2} \langle \tilde{Q}_i^n - I_i, \delta_a g_{i-a} \rangle + \sum_{i \in \mathbb{Z}^2} \|\delta_a g_{i-a}\|^2 = \quad (35)$$

$$2 \langle \delta_a, \sum_{i \in \mathbb{Z}^2} \epsilon_i^n g_{i-a} \rangle + \langle \delta_a^2, \sum_{i \in \mathbb{Z}^2} g_{i-a} g_{i-a} \rangle = \quad (36)$$

$$2 \langle \delta_a, C_{\mathbf{g}, \boldsymbol{\epsilon}^n}(a) \rangle + \langle \delta_a^2, C_{\mathbf{g}, \mathbf{g}}(0) \rangle. \quad (37)$$

The corresponding expression for $C_{\mathbf{g}, \boldsymbol{\epsilon}^n}$ is:

$$C_{\mathbf{g}, \boldsymbol{\epsilon}^n}(x) = C_{\mathbf{g}, \boldsymbol{\epsilon}}(x) + \sum_{k=1}^n \delta_{a^k} C_{\mathbf{g}, \mathbf{g}}(x-a^k). \quad (38)$$

5.3 Multiple simultaneous updates

If the search space is ignored and the formulation is analyzed in an abstract setting it becomes obvious that the *vertical* approach corresponds to an update of a single pixel, while the *horizontal* approach corresponds to an update of two pixels at the same time. This can be generalized further. Let N different pixels be updated per trial, and let there be n trials that have been accepted since $C_{\mathbf{g}, \boldsymbol{\epsilon}}$ has been updated. Let the pixels to be updated in the current trial be: $a_1^{n+1}, \dots, a_N^{n+1}$, and the accepted update at step k be at pixels: a_1^k, \dots, a_N^k . Let $\mathbf{Q}^0 = \mathbf{Q}$ be the original image. We define the sequence of images: $\mathbf{Q}^k : Q_i^k = Q_i^{k-1}, i \notin \{a_1^k, \dots, a_N^k\}$ and otherwise let $Q_{a_i^k}^k$ be given. Let $\delta_i^k = Q_{a_i^k}^k - Q_{a_i^k}^{k-1}$. Using the above notation we arrive at an expression for $C_{\mathbf{g}, \boldsymbol{\epsilon}^n}$:

$$C_{\mathbf{g}, \boldsymbol{\epsilon}^n}(x) = C_{\mathbf{g}, \boldsymbol{\epsilon}}(x) + \sum_{k=1}^n \sum_{i=1}^N \delta_i^k C_{\mathbf{g}, \mathbf{g}}(x-a_i^k). \quad (39)$$

The change in the energy due to the $n+1$ -st update is:

$$\delta^{n+1} = \|\tilde{\mathbf{Q}}^{n+1} - \mathbf{I}\|^2 - \|\tilde{\mathbf{Q}}^n - \mathbf{I}\|^2 = \quad (40)$$

$$\sum_{i \in \mathbb{Z}^2} \|\tilde{Q}_i^n - I_i + \sum_{j=1}^N \delta_j^{n+1} g_{i-a_j^{n+1}}\|^2 - \|\tilde{\mathbf{Q}}^n - \mathbf{I}\|^2 = \quad (41)$$

$$2 \sum_{i \in \mathbb{Z}^2} \langle \tilde{Q}_i^n - I_i, \sum_{j=1}^N \delta_j^{n+1} g_{i-a_j^{n+1}} \rangle + \sum_{i \in \mathbb{Z}^2} \|\sum_{j=1}^N \delta_j^{n+1} g_{i-a_j^{n+1}}\|^2 = \quad (42)$$

$$2 \sum_{j=1}^N \langle \delta_j^{n+1}, \sum_{i \in \mathbb{Z}^2} \epsilon_i^n g_{i-a_j^{n+1}} \rangle + \quad (43)$$

$$\sum_{j=1}^N \sum_{k=1}^N \langle \delta_j^{n+1} \delta_k^{n+1}, \sum_{i \in \mathbb{Z}^2} g_{i-a_j^{n+1}} g_{i-a_k^{n+1}} \rangle =$$

$$2 \sum_{j=1}^N \langle \delta_j^{n+1}, C_{\mathbf{g}, \boldsymbol{\epsilon}^n}(a_j^{n+1}) \rangle + \quad (44)$$

$$\sum_{j=1}^N \sum_{k=1}^N \langle \delta_j^{n+1} \delta_k^{n+1}, C_{\mathbf{g}, \mathbf{g}}(a_j^{n+1} - a_k^{n+1}) \rangle.$$

5.4 Implementation details

Leaky energy. Similar to the original paper [Analoui and Allebach 1992], in our extension δ was computed for a "leaky energy" which extended the support of the image by convolution. That is reflected in the fact that the sums are over \mathbb{Z}^2 . To rectify this, the sum needs to be limited to the support of \mathbf{I} . This would require clamped sums of the cross-correlation to be evaluated, which can also be precomputed but requires extra memory. The same holds for the cross-correlation with $\boldsymbol{\epsilon}$, where clamped terms are required near the image boundary.

Reflecting boundary conditions. Another desirable property may be a convolution such that it acts on the image extended to be reflected at the boundaries - this avoids artifacts near the borders. This can be achieved by including the relevant terms including pixels for which the kernel is partially outside of the support of \mathbf{I} . Care must be taken when expressing \tilde{Q}_i , however, since it may include the same updated pixel numerous times (especially if it is near the border). The same ideas apply for a toroidally extended convolution.

Further optimisations. Various other strategies have been proposed in the literature for improving the runtime of iterative error minimization approaches for halftoning.

In our algorithms we usually use a randomized initial state, however, it is possible to initialize the algorithms with the result of a dither matrix halftoning algorithm or error diffusion algorithm which would result in faster convergence [Analoui and Allebach 1992].

Another strategy involves partitioning the image in blocks. Instead of updating the pixels in raster or serpentine order, the blocks are updated simultaneously by keeping only the best update per block in each iteration. This has been reported to run 10+ times faster [Lieberman and Allebach 1997]. In the same paper [Lieberman and Allebach 1997], approximating the kernel with box functions has been proposed yielding a speed up of 6 times. Similarly, if the kernel is separable or can be approximated by a separable kernel,

the convolution can also be made considerably faster. A speed-up of an additional 30 times has been reported in [Koge et al. 2014] through the usage of a GPU.

Finally, several heuristics related to the the order in which pixels are iterated over have been proposed in [Bhatt et al. 2006].

5.5 Spatially varying kernels

We propose an optimisation for spatially varying kernels also. Let kernel \mathbf{g}_i be associated with pixel i . Let pixel a be updated to a new value Q'_a , while everywhere else the images match: $Q'_i = Q_i$, and $\delta_a = Q'_a - Q_a$. We denote $\tilde{Q}_i = \langle \mathbf{g}_i, \mathbf{Q} \rangle$, $\tilde{Q}'_i = \langle \mathbf{g}_i, \mathbf{Q}' \rangle = \tilde{Q}_i + g_{i,a} \delta_a$. Our goal is to evaluate the change in the energy due to the update:

$$\delta = \|\tilde{\mathbf{Q}}' - \mathbf{I}\|^2 - \|\tilde{\mathbf{Q}} - \mathbf{I}\|^2 = \quad (45)$$

$$\sum_{i \in \mathbb{Z}^2} \|\tilde{Q}_i - I_i + g_{i,a} \delta_a\|^2 - \|\tilde{\mathbf{Q}} - \mathbf{I}\|^2 = \quad (46)$$

$$2 \sum_{i \in \mathbb{Z}^2} \langle \epsilon_i, g_{i,a} \delta_a \rangle + \sum_{i \in \mathbb{Z}^2} \|g_{i,a} \delta_a\|^2 = \quad (47)$$

$$2 \langle \delta_a, \sum_{i \in \mathbb{Z}^2} \epsilon_i g_{i,a} \rangle + \langle \delta_a^2, \sum_{i \in \mathbb{Z}^2} g_{i,a} g_{i,a} \rangle. \quad (48)$$

In the above $C_{\mathbf{g}, \mathbf{g}}(a) = \sum_{i \in \mathbb{Z}^2} g_{i,a} g_{i,a}$ may be precomputed for every a , which yields a function with support $\text{supp}(C_{\mathbf{g}, \mathbf{g}}) = \bigcup_i \text{supp}(\mathbf{g}_i)$, and $C_{\mathbf{g}, \boldsymbol{\epsilon}}(a) = \sum_{i \in \mathbb{Z}^2} \epsilon_i g_{i,a}$ can also be recomputed after enough updates have been accepted.

Multiple accepted updates. Let a set of accepted updates results in the differences: $\{\delta_{a^1}, \dots, \delta_{a^n}\}$. And let $\boldsymbol{\epsilon}^n$ be the error image after the updates. We derive an expression for the efficient evaluation of $C_{\mathbf{g}, \boldsymbol{\epsilon}^n}$:

$$C_{\mathbf{g}, \boldsymbol{\epsilon}^n}(x) = \sum_{i \in \mathbb{Z}^2} \epsilon_i^n g_{i,x} = C_{\mathbf{g}, \boldsymbol{\epsilon}}(x) + \sum_{k=1}^n \delta_{a^k} \sum_{i \in \mathbb{Z}^2} g_{i,a^k} g_{i,x}. \quad (49)$$

An efficient computation of $C_{\mathbf{g}, \boldsymbol{\epsilon}^n}$ can then be achieved if the function $C_{\mathbf{g}, \mathbf{g}}(x, y) = \sum_{i \in \mathbb{Z}^2} g_{i,x} g_{i,y}$ is precomputed. Then, at step $n+1$ the change in energy is:

$$\delta^{n+1} = \|\tilde{\mathbf{Q}}^{n+1} - \mathbf{I}\|^2 - \|\tilde{\mathbf{Q}}^n - \mathbf{I}\|^2 = \quad (50)$$

$$2 \langle \delta_{a^{n+1}}, C_{\mathbf{g}, \boldsymbol{\epsilon}^n}(a^{n+1}) \rangle + \langle \delta_{a^{n+1}}^2, C_{\mathbf{g}, \mathbf{g}}(a^{n+1}) \rangle. \quad (51)$$

Multiple simultaneous updates. We derive an expression where an update consists of changing N pixels simultaneously, and we assume that n such updates have been accepted previously. We denote the differences of the pixels in update k : $\{\delta_1^k, \dots, \delta_N^k\}$. The expression for the change in the energy is given as:

$$\delta^{n+1} = \|\tilde{\mathbf{Q}}^{n+1} - \mathbf{I}\|^2 - \|\tilde{\mathbf{Q}}^n - \mathbf{I}\|^2 = \quad (52)$$

$$\sum_{i \in \mathbb{Z}^2} \|\tilde{Q}_i^n - I_i + \sum_{j=1}^N \delta_j^{n+1} g_{i,a_j^{n+1}}\|^2 - \|\tilde{\mathbf{Q}}^n - \mathbf{I}\|^2 = \quad (53)$$

$$2 \sum_{j=1}^N \langle \delta_j^{n+1}, C_{\mathbf{g}, \boldsymbol{\epsilon}^n}(a_j^{n+1}) \rangle + \sum_{i=1}^N \sum_{j=1}^N \langle \delta_i^{n+1} \delta_j^{n+1}, C_{\mathbf{g}, \mathbf{g}}(a_i^{n+1}, a_j^{n+1}) \rangle. \quad (54)$$

Where $C_{\mathbf{g},\mathbf{g}}(x, y) = \sum_{i \in \mathbb{Z}^2} g_{i,x} g_{i,y}$ is assumed to be precomputed, and $C_{\mathbf{g},\epsilon^n}$ can be computed as:

$$C_{\mathbf{g},\epsilon^n}(x) = C_{\mathbf{g},\epsilon}(x) + \sum_{k=1}^n \sum_{j=1}^N \delta_{a_j^k} C_{\mathbf{g},\mathbf{g}}(a_j^k, x). \quad (55)$$

6 RELATIONSHIP TO PREVIOUS WORK

We show that the recent publications [Georgiev and Fajardo 2016; Heitz et al. 2019; Heitz and Belcour 2019] on blue noise error distribution for path tracing, can be seen as special cases in our framework. This allows for a novel analysis and interpretation of the results in the aforementioned works. We also state the necessary assumptions and approximations necessary to get from our general formulation to the algorithms presented in the papers.

Classification. The proposed techniques can be divided into *a-priori* [Georgiev and Fajardo 2016; Heitz et al. 2019] and *a-posteriori* [Heitz and Belcour 2019]. The main difference is that for *a-priori* techniques broad assumptions are made on the integrand without relying on information from renderings of the current scene. The cited *a-priori* approaches describe ways for constructing offline optimized point sets/sequences. We denote the method in [Georgiev and Fajardo 2016] as BNDS (blue-noise dithered sampling), the method in [Heitz et al. 2019] as HBS (Heitz-Belcour Sobol), and the histogram and permutation method in [Heitz and Belcour 2019] as HBH and HBP respectively (Heitz-Belcour histogram/permutation).

Energy. HBH/HBP both rely on a blue noise dither matrix optimized while using a Gaussian kernel (through void-and-cluster [Ulichney 1993]). This kernel corresponds to the kernel in our framework \mathbf{g} . The optimisation of this dither matrix happens offline unlike in our iterative energy minimization algorithms. This imposes multiple restrictions while allowing for a lower runtime. On the other hand, the dither matrices in HBS and BNDS are optimized with respect to empirically motivated energies that cannot be related directly to what is used as energy in HBH and HBP. In the case of BNDS the energy does not even introduce an implicit integrand, and instead it is devised to represent a whole class of integrands. We propose to substitute those empirically motivated energies with a modified version of our energy. This allows an intuitive interpretation and relating *a-posteriori* approaches to *a-priori* approaches.

Search space. Another notable difference constitute the search spaces on which the different approaches operate. HBH selects a subset from a set of precomputed samples in each pixel, HBP permutes the assignment of sample sets to pixels, BNDS directly modifies the set of samples in each pixel, and HBS considers a search space made up of scrambling and ranking keys for a Sobol sequence. Working on the space of scrambling and ranking keys guarantees the preservation of the desirable integration qualities of the Sobol sequence used, and it should be clear that other methods can also be restricted to such a space. Clearly, a search space restriction diminishes the achievable blue noise quality. On the other hand, it makes sequences more robust to integrands for which those were not optimized.

7 A-POSTERIORI APPROACHES

In this section we analyze the permutation based approach (HBP) and the histogram sampling approach (HBH) proposed in [Heitz and Belcour 2019]. The two methods can be classified as dither matrix halftoning methods in our framework, that operate on a *horizontal* and *vertical* search space respectively. We make the approximations and assumptions necessary to get from our general formulation to HBP/HBH explicit.

We also note that *a-posteriori* methods lead to solutions that adapt to the current render by exploiting known information (e.g. previously rendered data, auxiliary buffers). They can generally produce better results than *a-priori* methods.

Both HBP and HBH rely on a blue noise dither matrix \mathbf{B} . Let \mathbf{B} be the optimized blue noise dither matrix resulting from the minimization of $E(\mathbf{B}) = \|\mathbf{g} * \mathbf{B}\|_2^2$ over a suitable search space. The kernel \mathbf{g} is the one used to generate the blue noise images for HBP/HBH. That is, the Gaussian kernel in the void-and-cluster method [Ulichney 1993]. Our analysis does not rely on the kernel being a Gaussian, or on the void-and-cluster optimization, this is simply the setting of the HBP/HBH method. In the more general setting any kernel is admissible.

7.1 Sorting step for the permutation approach

The permutation approach [Heitz and Belcour 2019] consists of two main parts: sorting (optimization), and retargeting (correcting for mispredictions). The sorting step in HBP can be interpreted as minimizing the energy:

$$E_{HBP}(\pi) = \|\pi(\mathbf{Q}) - f_2(\mathbf{B})\|_2^2, \forall f_2 : a < b \implies f_2(a) < f_2(b). \quad (56)$$

A global minimum of the above energy is achieved for a permutation π that matches the order statistics of \mathbf{Q} and \mathbf{B} . Thus our goal would be to get from the minimization of:

$$E(\pi) = \|\mathbf{g} * (\mathbf{Q}(\pi(\mathbf{S})) - \mathbf{I})\|_2^2 = \|\mathbf{g} * \epsilon(\pi(\mathbf{S}))\|_2^2, \quad (57)$$

to the minimization of Eq. (56) over a suitable search space (in practice it is limited to permutations within tiles).

We successively bound the error, while introducing the assumptions implicit to the HBP method. The bounds are not tight, however, the different error terms that we consider illustrate the major sources of error due to the approximation of the more general energy (Eq. (57)) with a simpler one (Eq. (56)). The substitution of the kernel convolution $\mathbf{g} * \cdot$ by a difference with a blue noise mask \mathbf{B} restricts the many possible blue noise error distributions towards which $\epsilon(\pi(\mathbf{S}))$ can go with a single one: \mathbf{B} . A global minimizer of the new simplified energy can thus be found by just sorting.

The closer the distributions of $\epsilon(\pi(\mathbf{S}))$ and $\alpha\mathbf{B}$, $\alpha > 0$ are locally, the lower this restriction error can be made. Notably, for a close to linear relationship between the samples and the integrand, and sufficiently many pixels, $\epsilon(\pi(\mathbf{S}))$ and $\alpha\mathbf{B}$ can be matched closely in practice. A different way to reduce the approximation error is to introduce a sufficient amount of different blue noise images and pick the one that minimizes the error. We start with the original energy (Eq. (57)) and bound it through terms that capture the main assumptions on which the model relies:

$$\begin{aligned}
& \|\mathbf{g} * \boldsymbol{\epsilon}(\pi(\mathbf{S}))\|_2 = \\
\min_{f_2} & \|\mathbf{g} * (\boldsymbol{\epsilon}(\pi(\mathbf{S})) - f_2(\mathbf{B}) + f_2(\mathbf{B}))\|_2 \leq \\
& \min_{\alpha > 0, f_2} \|\mathbf{g}\|_1 \|\boldsymbol{\epsilon}(\pi(\mathbf{S})) - f_2(\mathbf{B})\|_2 \\
& + \|\mathbf{g} * (f_2(\mathbf{B}) - \alpha \mathbf{B} + \alpha \mathbf{B})\|_2 \leq \\
& \min_{\alpha > 0, f_2} \|\mathbf{g}\|_1 \|\boldsymbol{\epsilon}(\pi(\mathbf{S})) - f_2(\mathbf{B})\|_2 \\
& + \|\mathbf{g}\|_1 \|(f_2(\mathbf{B}) - \alpha \mathbf{B})\|_2 + \alpha \|\mathbf{g} * \mathbf{B}\|_2.
\end{aligned} \tag{58}$$

In the above, f_2 is taken over the space of all strictly monotonically increasing functions, and $\alpha > 0$ is a real value used to provide an amplitude matching between $\boldsymbol{\epsilon}(\pi(\mathbf{S}))$ and \mathbf{B} (this allows for the second term to go to zero as the pointwise error goes to zero).

7.1.1 Third error term. We note that \mathbf{B} is precomputed offline in order to approximately minimize $E(\mathbf{B}) = \|\mathbf{g} * \mathbf{B}\|_2$. Thus, the third term reflects the quality of the blue noise achieved with respect to \mathbf{g} in the offline minimization. This error can be made small without a performance penalty since the optimization is performed offline. We factor out a multiplicative scaling factor $\alpha > 0$ in the blue noise quality term, to allow for the second term to go to zero. With this change, we can consider \mathbf{B} to be normalized in the range $[-1, 1]$ and we can encode the scaling in α .

7.1.2 Second error term. The second term reflects the error introduced by substituting a large search space (many local minima) with a small search space. It introduces the first implicit assumption of HBP by relating the first and third error terms (by using f_2 and α respectively) through the second error term. The assumption is that there exists a permutation for which $\boldsymbol{\epsilon}(\pi(\mathbf{S}))$ can be made close to $\alpha \mathbf{B}$, which would make the second term small. This holds in practice if the pixel-wise error is zero on average (unbiased estimator within each pixel), and we have a sufficiently large resolution/tiles: which results in a higher probability that pixels from $\boldsymbol{\epsilon}(\pi(\mathbf{S}))$ can match \mathbf{B} well. Then the term $\|\mathbf{g}\|_1 \|f_2(\mathbf{B}) - \alpha \mathbf{B}\|_2$ can be made small. We note that this is a generalization of the third optimality condition in [Heitz and Belcour 2019] (*correlation-preserving integrand*) since an integrand linear in the samples can also better match \mathbf{B} provided enough pixels. For a linear integrand the optimal f_2 is also a linear function (ideal correlation between samples and integrand). The main difference between a linear integrand and a nonlinear/discontinuous one, is the amount of sample sets/pixels necessary to match $f_2(\mathbf{B})$ well, given an initial white noise samples' distribution. So in practice there are 4 factors directly affecting the magnitude of the second term: the number of considered blue noise images, the size of the tiles, the correlation between samples and integrand (accounted for by f_2), the bias/consistency of the estimators.

We note that the number of considered pixels depends on the tile size in HBP, and the practical significance of this has been demonstrated through a canonical experiment in the main paper.

7.1.3 First error term. Before we proceed we need to further bound the first error term by substituting $\mathbf{Q}(\pi(\mathbf{S}))$ by $\pi(\mathbf{Q}(\mathbf{S}))$. As discussed in the main paper, this is achieved by introducing a difference term $\Delta(\pi) = \mathbf{Q}(\pi(\mathbf{S})) - \pi(\mathbf{Q}(\mathbf{S}))$, and then $\sqrt{E_{HBP}}$ is recovered.

The error there can be made arbitrarily small through f_2 (it is accounted for in the second term). Thus we only need to study the remaining error due to Δ . In the case of HBP, Δ is approximated by non-overlapping characteristic functions in each tile ($d(x, y) = \infty$, for x, y in different tiles). This means that the approximation error is zero within each tile if the integrands are the same within the tile and permutations act only within the tile, since $\Delta(\pi) = \mathbf{0}$. On the other hand, if this assumption is violated, mispredictions occur, usually resulting in white noise.

7.1.4 Δ term. HBP partitions screen space into a several tiles $\mathcal{R}_1, \dots, \mathcal{R}_K$, and permutations are only over the pixel values in a tile. Having the partition induced by the tiling we can bound the first term:

$$\|\boldsymbol{\epsilon}(\pi(\mathbf{S})) - f_2(\mathbf{B})\|_2 \leq \sum_{k=1}^K \|\boldsymbol{\epsilon}_k(\pi_k(\mathbf{S}_k)) - f_2(\mathbf{B})\|_2. \tag{59}$$

Since additionally the permutations are optimized for the pixel values instead of the sample sets (which saves re-rendering operations), then there is an assumption that within each tile \mathcal{R}_k the following holds (we denote $\mathbf{A}_k = \mathbf{A}|_{\mathcal{R}_k}$):

$$\mathbf{Q}_k(\pi_k(\mathbf{S}_k)) = \pi_k(\mathbf{Q}_k(\mathbf{S}_k)). \tag{60}$$

Consequently it follows that $I_i = I_j, \forall i, j \in \mathcal{R}_k$.

This assumption can be identified with the 4-th optimality condition proposed in [Heitz and Belcour 2019]: *screen-space coherence*. As discussed, the search space restriction to the tiles corresponds to an approximation of the Δ term in our framework by characteristic functions: $d_k(x, y) = \infty, x \in \mathcal{R}_k, y \notin \mathcal{R}_k$ and $d_k(x, y) = 0, x, y \in \mathcal{R}_k$. To account for the actual error when the assumption is violated we introduce an additional error term per tile: $\Delta_k = \mathbf{Q}_k(\pi_k(\mathbf{S}_k)) - \pi_k(\mathbf{Q}_k(\mathbf{S}_k))$, then we have the bound:

$$\begin{aligned}
& \|\boldsymbol{\epsilon}_k(\pi_k(\mathbf{S}_k)) - f_2(\mathbf{B}_k)\|_2 = \\
& \|\pi_k(\mathbf{Q}_k(\mathbf{S}_k)) - \mathbf{I}_k - f_2(\mathbf{B}_k) + \Delta_k\|_2 \leq \\
& \|\pi_k(\mathbf{Q}_k(\mathbf{S}_k)) - \mathbf{I}_k - f_2(\mathbf{B}_k)\|_2 + \|\Delta_k\|_2.
\end{aligned} \tag{61}$$

This means that even if all of the previous error terms are made small, including $\|\pi_k(\boldsymbol{\epsilon}_k(\mathbf{S}_k)) - f_2(\mathbf{B}_k)\|_2$, the error may still be large due to $\|\Delta_k\|_2$. We refer to a large error due to the delta term as *misprediction* - that is, a mismatch between the predicted error distribution from the minimization of $\|\pi_k(\boldsymbol{\epsilon}_k(\mathbf{S}_k)) - f_2(\mathbf{B}_k)\|_2$ and the actual error distribution resulting from the above permutation applied to $\boldsymbol{\epsilon}_k(\pi_k(\mathbf{S}_k))$. The best way to identify mispredictions is to compare the predicted image $\pi_k(\mathbf{Q}_k(\mathbf{S}_k))$ and the image rendered with the same permutation for the sample sets $\mathbf{Q}_k(\pi_k(\mathbf{S}_k))$. A misprediction occurring means that the assumption made to approximate Δ was incorrect ($\Delta_k \neq \mathbf{0}$ for some tile \mathcal{R}_k), equivalently the optimality condition of *screen-space coherence* is not satisfied.

Avoiding mispredictions. In practice mispredictions often occur for larger tile sizes, since it is hard to guarantee that the integrand remains similar over each tile. On the other hand, larger tiles allow for a better blue noise as long as $\Delta_k = \mathbf{0}$ in each tile, thus larger tiles are desirable. The method fails even more often near edges, since even for small tile sizes it allows swapping pixels over an edge. A straightforward improvement involves partitioning the domain by

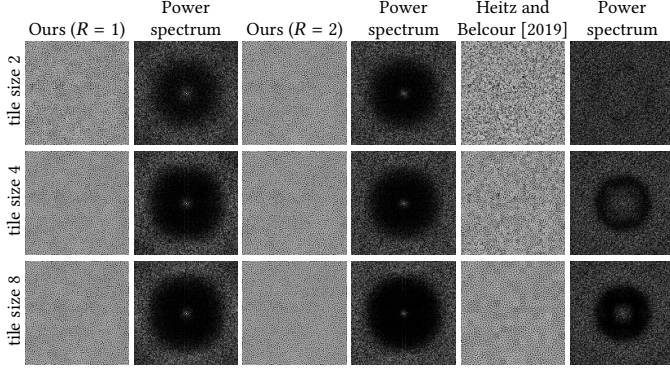


Fig. 2. Here we showcase the effect of tile size on the quality of blue noise. We also demonstrate the effect of a larger search neighbourhood R in our optimization (Alg. 2). For our case, we consider disk neighbourhoods so that they are contained within Heitz and Belcour’s tiles in terms of size, but they can also overlap due to our formulation. From left-to-right, the input white noise texture is optimized using our relocation algorithm. The last two columns are from Heitz and Belcour’s [2019] method. The corresponding power spectra of these optimized images (128×128) are also shown.

respecting edges. More involved methods may take into account normals, depth, textures, etc.

7.1.5 E_{HBP} error term. The final step involves the minimization of the energy in Eq. (61). Since different tiles do not affect each other the minimization can be performed per tile (we adopt the assumption from HBP $\Delta_k = \mathbf{0}$):

$$\begin{aligned} \pi_k^* \in \arg \min_{\pi_k} \|\pi_k(\mathbf{Q}_k(\mathbf{S}_k)) - \mathbf{I}_k - f_2(\mathbf{B}_k)\|_2 = \\ \arg \min_{\pi_k} \|\pi_k(\mathbf{Q}_k(\mathbf{S}_k)) - f_2(\mathbf{B}_k)\|_2^2. \end{aligned} \quad (62)$$

We have dropped the term \mathbf{I}_k since it doesn’t affect the set of minimizers (\mathbf{I}_k is assumed constant in each tile). As discussed in Eq. (56), a global minimum is given by matching the order statistics of \mathbf{Q}_k to the order statistics of $f_2(\mathbf{B})$ (we note that the order statistics of \mathbf{B}_k do not change from the application of f_2 since it is a strictly increasing function). This is equivalent to performing the sorting pass described in [Heitz and Belcour 2019]. A minor optimization would be to pre-sort \mathbf{B} and instead store the sorted indices.

Tiling effect. In Fig. 2 we compare the effect of the tile size. In our approach, the “tiles” can be defined per pixel, can have arbitrary shapes, and are overlapping, the last being crucial for achieving a good blue noise distribution. We consider white-noise with mean 0.5 (which is an ideal scenario for Heitz and Belcour’s method) and compare various tile sizes. For a fair comparison, our tile radius r corresponds similar tile-size in the permutation [2019] approach. The power-spectrum profiles confirm the better performance of our method. Retargeting [2019] cannot improve the quality of the permutation approach either, since no misprediction can occur ($\Delta = 0$). The adverse effect of tiling is exacerbated in practice since, for images which are not smooth enough in screen space, tiles of smaller sizes need to be considered.

Custom surrogate. The \mathbf{I}_k term doesn’t need to be assumed constant in fact. If it is assumed constant, that is equivalent to picking a tile-constant surrogate, however, a custom surrogate may be provided instead. Then one would simply minimize the energy:

$$\|\pi_k(\mathbf{Q}_k(\mathbf{S}_k)) - (\mathbf{B}_k + \mathbf{I}_k)\|_2^2. \quad (63)$$

The energy has a different minimizer than the original HBP energy, but the global minimum can be found efficiently through sorting once again.

7.2 HBP retargeting

The retargeting pass in HBP achieves two things. It introduces new possible target solutions through new blue noise images, and it corrects for mispredictions. The first is not so much a result of the retargeting, as it is of varying the blue noise image every frame. Ideally several blue noise images would be considered in a single frame, and the best image would be chosen per tile (in that case one must make sure that there are no discontinuities between the blue noise images’ tiles) in order to minimize the second term in Eq. (58). Instead, in HBP this is amortized over several frames.

The more important effect of retargeting is correcting for mispredictions, by transferring the recomputed correspondence between sample set and pixel value (achieved through re-rendering) to the next frame. This allows reducing the error due to the approximation of Δ (when the piecewise-tile constancy assumption on the integrand is violated). Note however, that this is inappropriate if there is a large temporal discontinuity between the two frames.

Implementation details. Retargeting requires a permutation that transforms the blue noise image in the current frame into the blue noise image of the next frame [Heitz and Belcour 2019]. This permutation is applied on the optimized seeds to transfer the learned correspondence between sample sets and pixel values to the next frame. Implicitly, this transforming permutation also relies on a screen space integrand similarity assumption, since there is no guarantee that the corresponding values from the swap will match, possibly incurring a misprediction once again (it can be modeled by an additional Δ term). In HBP [Heitz and Belcour 2019] the maximum radius of travel of each pixel in the permutation is set to 6 pixels. This has a direct effect on the approximation of Δ , as the travel distance of a pixel is allowed to extend beyond the original tile bounds. In the worst case scenario a pixel may allowed to travel a distance of $\sqrt{t_x^2 + t_y^2} + 6$ pixels, where t_x, t_y are the dimensions of the tiles. An additional error is introduced since the retargeting pass does not produce the exact blue noise image used in the next frame, but some image that is close to it [Heitz and Belcour 2019]. This seems to be done purely from memory considerations since it allows one blue noise image to be reused by translating it toroidally each frame to produce the blue noise image for the next frame.

Relationship to our horizontal approach. Our horizontal approach does not require a retargeting pass. It can directly continue with the optimized sample sets and pixel values from last frame. There is also no additional travel distance for a matching permutation as

in retargeting, which further minimizes the probability of misprediction. Thus, it inherently and automatically produces all of the advantages of retargeting while retaining none of its disadvantages.

7.3 Histogram sampling approach

The histogram sampling approach from Heitz and Belcour can be interpreted as both a dithering and a sampling method. We study the dithering aspect to better understand the quality of blue noise achievable by the method.

Algorithm analysis. The sampling of an estimate in each pixel by using the corresponding mask value to the pixel can be interpreted as performing a mapping of the mask's range and then quantizing to the closest estimate. In HBH each estimate is equally likely to be sampled (if a random mask is used), which implies a transformation that maps equal parts of the range to each estimate. Let $Q_{k,1}, \dots, Q_{k,N}$ be the greyscale estimates in pixel k sorted in ascending order. Let the range of the blue noise mask be in $[0,1]$. Then the range is split into N equal subintervals: $[0, \frac{1}{N}), \dots, [\frac{N-1}{N}, 1]$ which respectively map to $[Q_1, \frac{Q_1+Q_2}{2}), \dots, [\frac{Q_{i-1}+Q_i}{2}, \frac{Q_i+Q_{i+1}}{2}), \dots, [\frac{Q_{N-1}+Q_N}{2}, Q_N]$. If the quantization rounds to the closest estimate, then the above mapping guarantees the desired behaviour. We note that since the estimates in each pixel can have different values, the mapping for each pixel may be different. We will denote the above mapping through f . Then the mapping plus quantization problem in a pixel k may be formulated as:

$$\min_{i \in \{1, \dots, N\}} |Q_{k,i} - f_k(B_k)|. \quad (64)$$

Note that the minimization in each pixel is independent, and it aims to minimize the distance between the estimates and the remapped value from the blue noise mask. If the set of estimates are assumed to be the same across pixels, and are also assumed to be spaced regularly, then f is only a linear remapping, which effectively transfers the spectral properties of \mathbf{B} onto the optimized image. Notably, the former is the *screen-space coherence* assumption from HBP, while the latter is the *correlation-preserving integrand* assumption. Thus we have seen that for optimal results the HBH method relies on exactly the same assumption as the HBP method (while our *vertical* iterative minimization approach lifts both assumptions).

Disadvantages. One of the key points is that the error distribution and not the signal itself ought to ideally be shaped as \mathbf{B} . This is actually the case even in the above energy. From the way f was chosen it follows that the surrogate is equivalent to $f(0.5)$ which can be identified as the image made of the median of the sorted estimates within each pixel. This is the case since if the target surrogate of \mathbf{B} (during the offline optimization) was assumed to be 0.5, then after the mapping it is $f(0.5)$. Generally, this is a very bad surrogate in the context of rendering, and it generally increases the error compared to the averaged image, making the method impractical.

Another notable disadvantage is that all estimates are considered with an equal weight. This means that outliers are as likely to be picked as estimates closer to the surrogate. This results in fireflies appearing even when those were not present in the averaged imaged. Compared to classical halftoning, where only the *closest* lower and

upper quantization levels are considered, HBH does not minimize the magnitude of the error to the surrogate.

Finally, the two assumptions of: *screen-space coherence* and *correlation-preserving integrand*, generally do not hold in practice. Estimates cannot be assumed to match between pixels (especially if samples are taken at random), and they cannot be assumed to be uniformly distributed, which implies that f is not linear. This greatly impacts the quality of the result, especially if it is compared to *adaptive* approaches such as our *vertical* error diffusion approach and our iterative minimization techniques (see the experiments in the main paper).

Generalization. The method can be generalized to take a custom surrogate instead of the one constructed by the median of the estimates within each pixel. This is achieved by splitting the per pixel set of estimates into two parts: (greyscale) estimates greater than the value of the (greyscale) surrogate in the current pixel, and estimates lower than it. Then the mapping f_k for the current pixel k maps values in $[0, 0.5)$ to the lower set, and values in $[0.5, 1]$ to the higher set, such that $f_k(0.5) = I_k$. The original method is recovered if the surrogate is chosen to be the implicit one for the original histogram sampling method and if the appropriate corresponding mapping f is kept.

The approach can be extended further by setting different probabilities for the different estimates. The original histogram sampling method correspond to setting the same probability for sampling every estimate, equivalently: equal sized sub-intervals from $[0, 1]$ map to each estimate. Classical dither matrix halftoning can be interpreted as setting an equal probability for the closest to the surrogate upper and lower estimates, while every other estimate gets a zero probability. Equivalently: equal sub-intervals from $[0, 1]$ map to the two aforementioned estimates while no part of the interval maps to the remaining estimates. Generally a custom probability can be assigned to each estimate: p_1, \dots, p_N , by having the intervals $[0, p_1), \dots, [\sum_{k=1}^{N-1} p_k, 1]$ map to Q_1, \dots, Q_N (after quantization). We note that an unbiased image can be recovered only if there is a map to every estimate.

8 A-PRIORI APPROACHES

We discuss current state of the art *a-priori* approaches [Georgiev and Fajardo 2016; Heitz et al. 2019] and their relation to our framework, as well as insights regarding those.

8.1 HBS

In Heitz et al.'s work, a scrambling energy and a ranking energy have been proposed (note that those energies are maximized and not minimized):

$$E_s = \sum_{i,j} \exp\left(-\frac{\|i-j\|_2^2}{2\sigma^2}\right) \|E_i - E_j\|_2^2 \quad (65)$$

$$E_r = \sum_{i,j} \exp\left(-\frac{\|i-j\|_2^2}{2\sigma^2}\right) (\|E_i^1 - E_j^1\|_2^2 + \|E_i^2 - E_j^2\|_2^2) \quad (66)$$

$$E_i = (e_{1,i}, \dots, e_{T,i}) \quad (67)$$

$$e_{t,i}(S_i) = \frac{1}{|S_i|} \sum_{k=1}^{|S_i|} f_t(p_{i,k}) - \int_{[0,1]^D} f_t(x) dx \quad (68)$$

$$S_i = \{p_{i,1}, \dots, p_{i,M_i}\}. \quad (69)$$

The upper indices in E_i^1, E_i^2 indicate that the two energies are evaluated with different subsets of the sample set S_i in the pixel i . The f_t are taken from an arbitrary set of functions (in the original paper those are random Heaviside functions). The described form of the energies has been partially motivated by the energy in [Georgiev and Fajardo 2016]. This doesn't allow for a straightforward interpretation or a direct relation to the (implicit) energy used for *a-posteriori* approaches in [Heitz and Belcour 2019].

Scrambling energy. We modify E_s in order to relate it to the energy in our framework and to provide a meaningful interpretation:

$$E'_s = \sum_{t=1}^T w_t \|\mathbf{g} * \mathbf{Q}_t(\mathbf{S}) - \mathbf{I}_t\|_2^2, \quad (70)$$

$$Q_{t,i}(\mathbf{S}) = \frac{1}{|S_i|} \sum_{k=1}^{|S_i|} f_t(p_{i,k}), \quad I_{t,i} = \int_{[0,1]^D} f_t(x) dx. \quad (71)$$

We have relaxed the Gaussian kernel to an arbitrary kernel \mathbf{g} and absorbed it into the norm. More importantly we have removed the heuristic dependence of error terms on their neighbours, and instead the coupling happens through the kernel itself. Finally, we have introduced weights w_1, \dots, w_T that allow assigning different importance to different integrands. Thus, this is a weighted average of our original energy applied to several different integrands, matching our *a-priori* approach (Eq. (1)). Through this formulation a direct relationship to the *a-posteriori* methods can be established, and it can be motivated in the context of both the human visual system and denoising. Particularly, the scrambling energy E'_s is over the space of scrambling keys, which allow permuting the assignment of sample sets. This is in fact the *horizontal* setting from our formulation in the main paper. The space can be extended further if the scrambling keys in each dimension are different (as in HBS). The same can be done in *a-posteriori* methods, if the optimization is performed in each dimension as discussed in Section 4.

Ranking energy. The ranking keys in HBS describe the order in which samples are consumed. This is useful for constructing progressive *a-priori* methods. Notably, the order in which samples will be introduced can be optimized. Having a sequence of sample sets in each pixel: $S_{i,1} \subset \dots \subset S_{i,M} \equiv S_i$ and respectively the images formed by those: $\mathbf{S}_1, \dots, \mathbf{S}_M$, the progressive energy may be constructed as:

$$E'_r = \sum_{k=1}^M w_k \|\mathbf{g} * \mathbf{Q}(\mathbf{S}_k) - \mathbf{I}\|_2^2. \quad (72)$$

The quality at a specific sample count corresponding to \mathbf{S}_k is controlled through the weight w_k . The original energy maximizing the quality of the full set is retrieved for $(w_1, \dots, w_{M-1}, w_M) = (0, \dots, 0, 1)$. Since the sample sets $S_1, \dots, S_{i,M}$ are optimized by choosing samples from S_i this can be seen as a *vertical* method. Finally, the ranking keys can also be defined per dimension, which can be related to *a-posteriori* methods through the suggested dimensional decomposition in Section 4.

8.2 Blue-noise dithered sampling energy

In Georgiev and Fajardo's work, in order to get an optimized (multi-channel) blue noise mask, the following energy has been proposed:

$$E(p_1, \dots, p_N) = \sum_{i \neq j} \exp\left(-\frac{\|i-j\|^2}{\sigma^2}\right) \exp\left(-\frac{\|p_i - p_j\|^{d/2}}{\sigma_s^2}\right), \quad (73)$$

which bears some similarity to the weights of a bilateral filter. In the above i, j are pixel coordinates, and p_i, p_j are d -dimensional vectors associated with i, j , let the image formed by those vectors be \mathbf{S} . The energy aims to make samples p_i, p_j distant ($\|p_i - p_j\|$ must be large) if they are associated with pixels which are close ($\|i - j\|$ is small).

Relation to our framework. Even though the energy is heuristically motivated, we can very roughly relate it to our framework. The above energy implicitly assumes classes of integrands $\mathbf{Q}_1, \dots, \mathbf{Q}_T$, such that close samples p_i, p_j are mapped to close values $Q_{i,t}(p_i), Q_{j,t}(p_j)$, and distant samples are mapped to distant values. Notably, the form of the energy doesn't change over screen-space, so the same can be implied about the integrands. One such class is the class of bi-Lipschitz functions. The bound can be used to relate a modified version of the original energy, to an energy of the form:

$$E_{\mathbf{Q}_t} = \sum_{i \neq j} \exp\left(-\frac{\|i-j\|^2}{\sigma^2}\right) \exp\left(-\frac{C \|Q_{i,t}(p_i) - Q_{j,t}(p_j)\|^{d/2}}{\sigma_s^2}\right). \quad (74)$$

Thus, the original energy can indeed be interpreted as reasonable for a whole class of sufficiently smooth integrands, instead of an energy that works very well with one specific integrand.

A similar thing can be achieved in our framework, if the weighted energy is considered:

$$E'(\mathbf{S}) = \sum_{t=1}^T w_t \|\mathbf{g} * \mathbf{Q}_t(\mathbf{S}) - \mathbf{I}_t\|_2^2. \quad (75)$$

The kernel \mathbf{g} can be a Gaussian with standard deviation σ , as in the original energy, or it can be relaxed to an arbitrary desired kernel. $\mathbf{Q}_1, \dots, \mathbf{Q}_T$ are representative integrands that satisfy the discussed smoothness requirements, and w_t are associated weights assigning different importance to the integrands. Finally, the reference images are given by the integrals $\mathbf{I}_t = \int_{[0,1]^d} \mathbf{Q}_t(x) dx$.

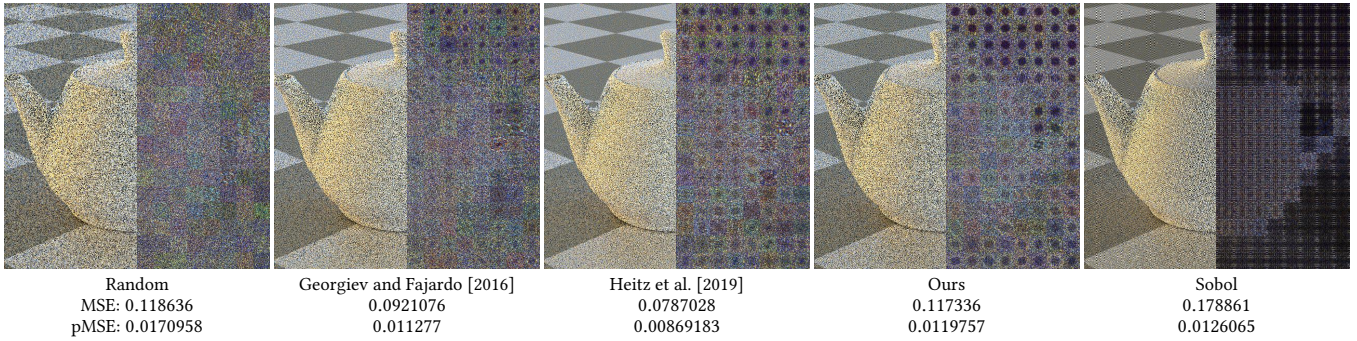


Fig. 3. A comparison illustrating that even a sampling sequence formed by a stack of blue noise images (Ours) yields a good distribution (note the tiled error spectra). The integration error is higher however, degrading the quality. This is the case because the assumed integrand is far from linear in each dimension (see *Extension* in Section 8.3). The images use 4 samples per pixel, and the degradation of the spectral properties with the number of samples is clear for [Georgiev and Fajardo 2016] and even [Heitz et al. 2019], while it is not so much the case for Ours. This demonstrates that different methods offer a different trade-off between integration error and distribution for arbitrary integrands. Constraining the search space to using toroidal shifts or scrambling and ranking keys restricts the achievable blue noise distribution.

It should be clear that this is a weighted average constructed from the standard energy in our framework applied to a set of integrands. There are a number of benefits of such an explicit formulation. Most importantly, it allows for *a-priori* methods to be studied in the same framework as *a-posteriori* approaches. Additionally, explicit control is provided over the set of integrands and the kernel in a manner that allows for a straightforward interpretation.

8.3 Blue-noise dithered sampling algorithm

The second contribution of Georgiev and Fajardo’s work is a sampler which relies on an image optimized with Eq. (73) and uses it to achieve a blue noise distribution of the rendering error. We summarize the algorithm and discuss some details related to it.

Algorithm. Let \mathbf{B} be an image (with d -channels) optimized by minimizing Eq. (73) over a suitable search space. Let $\mathcal{P} = \{p_1, \dots, p_N\}$ be a sequence of d -dimensional points. Within each pixel i the sample set S_i is constructed, such that:

$$p_j \in \mathcal{P} \implies p_{i,j} \in S_i : p_{i,j} = (p_j + B_i^*) \bmod 1. \quad (76)$$

The sequence \mathcal{P} can be constructed by using various samplers (e. g., random, low-discrepancy, blue-noise, etc.). The construction of the new points for pixel i can be interpreted either as toroidally shifting the sequence \mathcal{P} by B_i or equivalently as toroidally shifting the sequence $\{B_i, \dots, B_i\}$ by \mathcal{P} .

The sequences constructed within each pixel are used to estimate the integral in the usual manner. Since a finite number of dimensions d are optimized the suggestion is to distribute the constructed sequences over smoother dimensions, while other dimensions may use a standard sampler.

Effect of the toroidal shift. Let us consider a linear one-dimensional integrand $f(q) = \alpha q + \beta$ that does not vary in screen space, and a sequence \mathcal{P} with a single point p . Furthermore, if we assume $p = 0$, then the error is given by:

$$Q(\mathbf{B}) - I = \alpha \mathbf{B} + \beta - I. \quad (77)$$

Since Q does not vary in screen space, then I also doesn’t. Then the power spectrum of the error (excluding the DC) matches the power spectrum of \mathbf{B} up to the multiplicative factor α^2 . Then, under the assumption that the integrand is linear, does not vary in screen space, and there is no toroidal shift, the power spectral properties of \mathbf{B} are transferred ideally to the error.

On the other hand, if p is chosen to be non-zero, then the spectral characteristics of the image $((\mathbf{B} + p) \bmod 1)$ will be transferred instead. We have empirically verified that even with a very good quality blue noise image \mathbf{B} the toroidal shift degrades its quality due to the introduced discontinuities. Thus, even in the ideal case of a constant in screen space linear 1-D integrand, toroidal shifts degrade the quality.

Effect of using multiple samples. Let us consider the same integrand $f(q) = \alpha q + \beta$, which we have identified as being ideal for transferring the spectral characteristics of \mathbf{B} to the error. And let us assume that we are given several samples: $\mathcal{P} = \{p_1, \dots, p_N\}$, and we have constructed the sample set image \mathbf{S} through toroidal shifts with \mathbf{B} . Then the error is:

$$Q_i(S_i) - I_i = \frac{\alpha}{N} \sum_{k=1}^N p_{k,i} + \beta - I_i. \quad (78)$$

The power spectrum of the error thus matches the power spectrum of the image $A_i = \sum_{k=1}^N p_{k,i}$ (excluding the DC) up to a multiplicative factor. For a random point sequence \mathcal{P} the more points are considered, the closer to white noise \mathbf{A} becomes. This is further exacerbated by the discussed discontinuities introduced by the toroidal shifts.

Extension. We have argued that both toroidal shifts and increasing the number of samples has a negative effect on transferring the spectral properties of \mathbf{B} even in an ideal scenario. Naturally the question arises whether this can be improved. Our proposal is the direct optimisation of point sets without the application of a toroidal shift.

For the discussed example this entails constructing a sequence of N images $\mathbf{B}_1, \dots, \mathbf{B}_N$ such that $\mathbf{A}_k = \sum_{j=1}^k \mathbf{B}_j$ is a blue noise image. Then the error has the (blue noise) spectral characteristics of \mathbf{A}_k at each sample count:

$$Q_i(B_{1,i}, \dots, B_{k,i}) - I_i = \frac{\alpha}{k} \sum_{j=1}^k B_{j,i} + \beta - I_i. \quad (79)$$

9 EXTRA RESULTS

REFERENCES

- Mostafa Analoui and Jan P. Allebach. 1992. Model-based halftoning using direct binary search. In *Human Vision, Visual Processing, and Digital Display III*, Bernice E. Rogowitz (Ed.), Vol. 1666. International Society for Optics and Photonics, SPIE, 96–108. <https://doi.org/10.1117/12.135959>
- Sagar Bhatt, John Sabino, John Harlim, Joel Lepak, Robert Ronkese, and Chai Wah Wu. 2006. Comparative study of search strategies for the direct binary search image halftoning algorithm. In *NIP22 (International Conference on Digital Printing Technologies)*, 244–247. International Conference on Digital Printing Technologies ; Conference date: 17-09-2006 Through 22-09-2006.
- Iliyan Georgiev and Marcos Fajardo. 2016. Blue-noise Dithered Sampling. In *ACM SIGGRAPH 2016 Talks (Anaheim, California) (SIGGRAPH '16)*. ACM, New York, NY, USA, Article 35, 1 pages. <https://doi.org/10.1145/2897839.2927430>
- Eric Heitz and Laurent Belcour. 2019. Distributing Monte Carlo Errors as a Blue Noise in Screen Space by Permuting Pixel Seeds Between Frames. *Computer Graphics Forum* (2019). <https://doi.org/10.1111/cgf.13778>
- Eric Heitz, Laurent Belcour, Victor Ostromoukhov, David Coeurjolly, and Jean-Claude Iehl. 2019. A Low-Discrepancy Sampler that Distributes Monte Carlo Errors as a Blue Noise in Screen Space. In *SIGGRAPH'19 Talks*. ACM, Los Angeles, United States. <https://hal.archives-ouvertes.fr/hal-02150657>
- James T. Kajiya. 1986. The Rendering Equation. In *SIGGRAPH '86*, Vol. 20. 143–150.
- Hiroaki Koge, Yasuaki Ito, and Koji Nakano. 2014. A GPU Implementation of Clipping-Free Halftoning Using the Direct Binary Search. In *Algorithms and Architectures for Parallel Processing*, Xian-he Sun, Wenyu Qu, Ivan Stojmenovic, Wanlei Zhou, Zhiyang Li, Hua Guo, Geyong Min, Tingting Yang, Yulei Wu, and Lei Liu (Eds.). Springer International Publishing, Cham, 57–70.
- D. J. Lieberman and J. P. Allebach. 1997. Efficient model based halftoning using direct binary search. In *Proceedings of International Conference on Image Processing*, Vol. 1. 775–778 vol.1. <https://doi.org/10.1109/ICIP.1997.648077>
- Robert A. Ulichney. 1993. Void-and-cluster method for dither array generation, Vol. 1913. <https://doi.org/10.1117/12.152707>

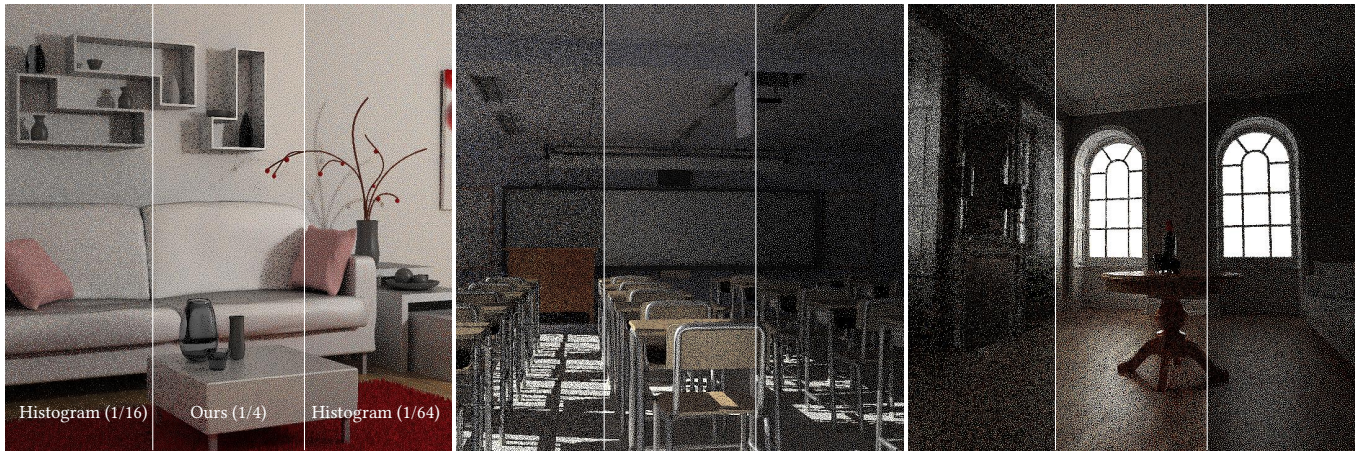


Fig. 4. We compare Heitz and Belcour’s histogram sampling method to our *vertical* iterative minimization on additional scenes. We provide 4 times and 16 times more samples for the histogram method, where each method picks one out of all of its allocated samples in each pixel. Despite the fact that our method may use 16 times less samples it still outperforms the histogram sampling approach. This is mainly due to the implicit surrogate and the suboptimal dithering inherent to the histogram sampling approach.

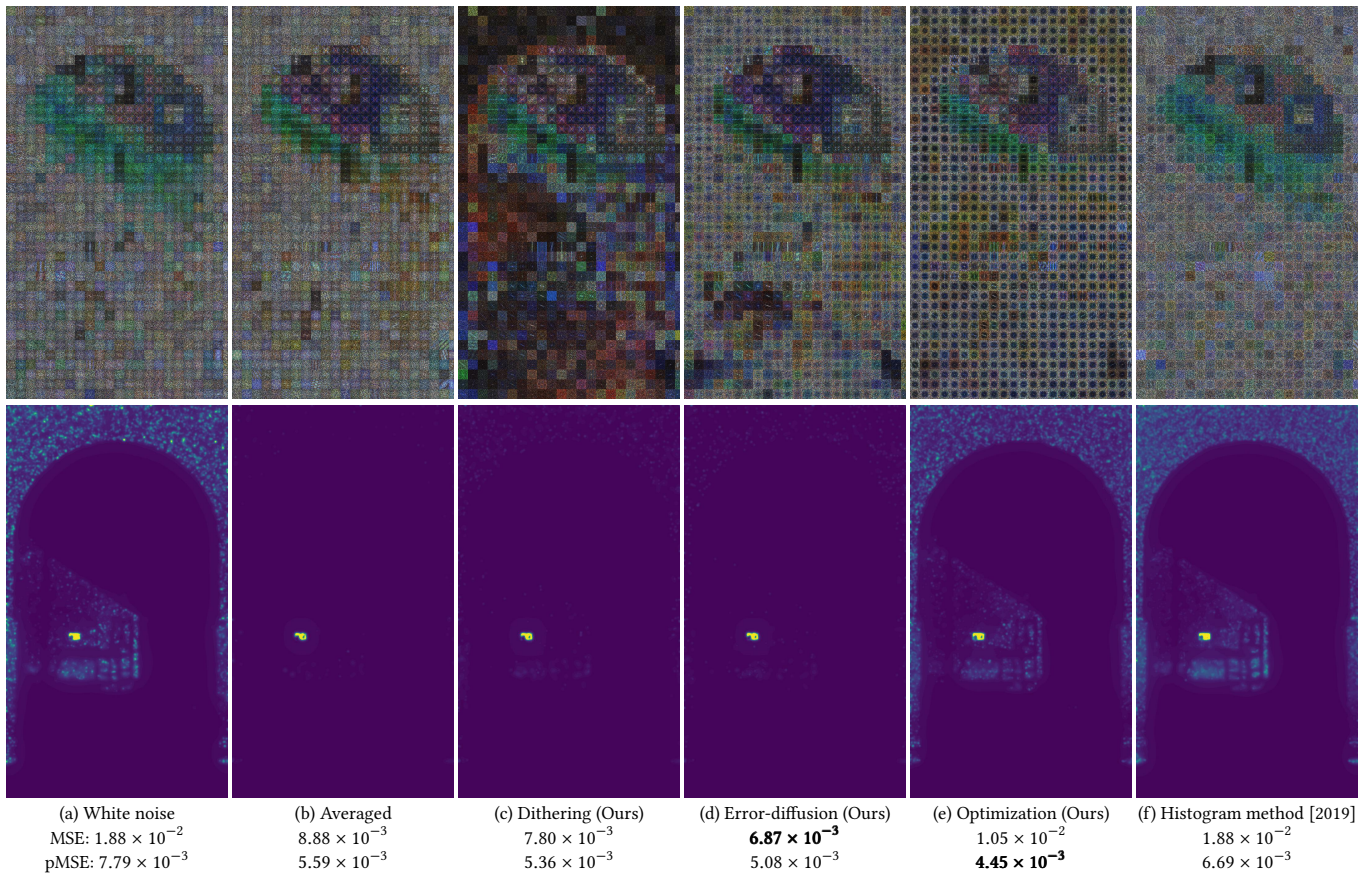


Fig. 5. In the main paper we compare all vertical methods on *The Wooden Staircase* scene. All of our methods achieve a better pMSE than the baseline (the averaged image), while the histogram sampling method increases the error both in terms of MSE and pMSE. The tiled error power spectra images confirm the pMSE ranking and provide a visualization of the local pMSE distribution. We also show S-CIELAB error visualizations which suggest that pointwise error is heavily weighted in S-CIELAB, which doesn’t make it a very good predictor for the perceptual quality related to the noise distribution, unlike HDR-VDP-2.

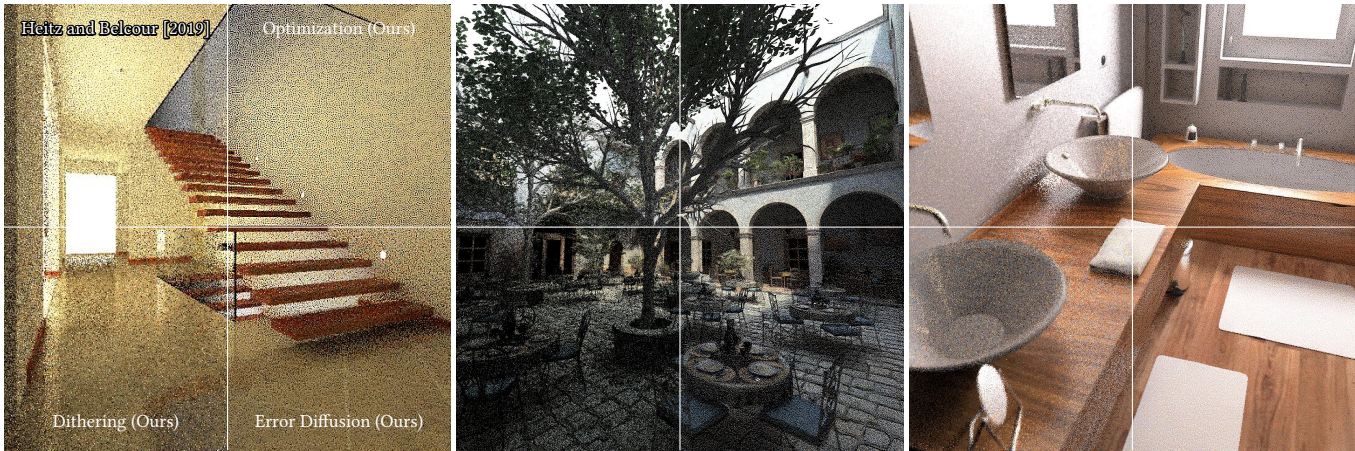


Fig. 6. Additional scenes comparing our *vertical* methods against Heitz and Belcour’s permutation approach. The images are rendered at 4 samples per pixel. The permutation approach uses 16 (static) frames with retargeting to improve mispredictions, however this still does not eliminate all of the mispredictions. This is especially evident in the *Bathroom* scene.

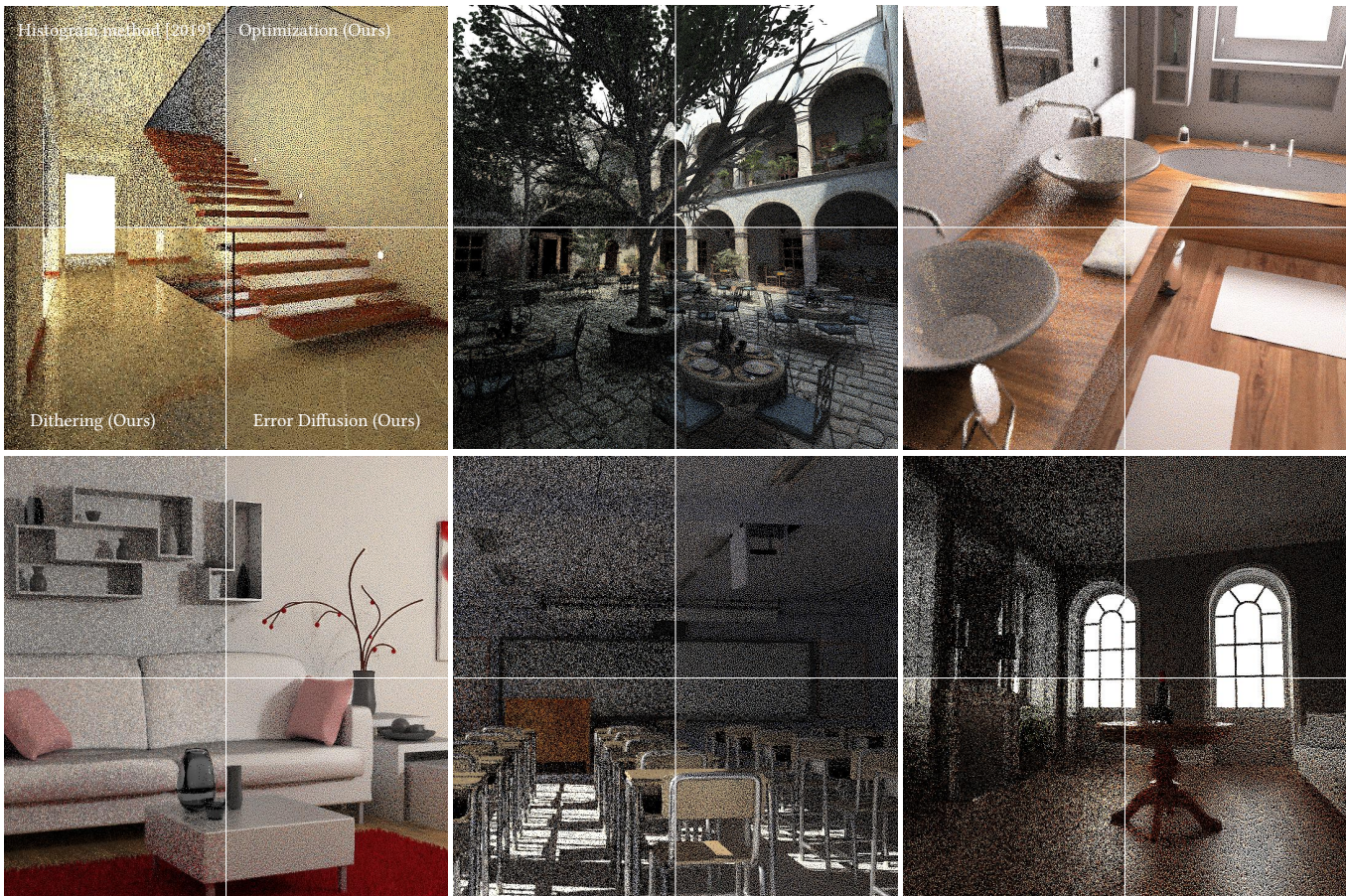


Fig. 7. All *vertical* methods from the main paper are compared at 4 samples per pixel. The ranking based on our error metrics is (best last): histogram sampling, dithering, error diffusion, iterative minimization. This also matches our perceptual evaluation.

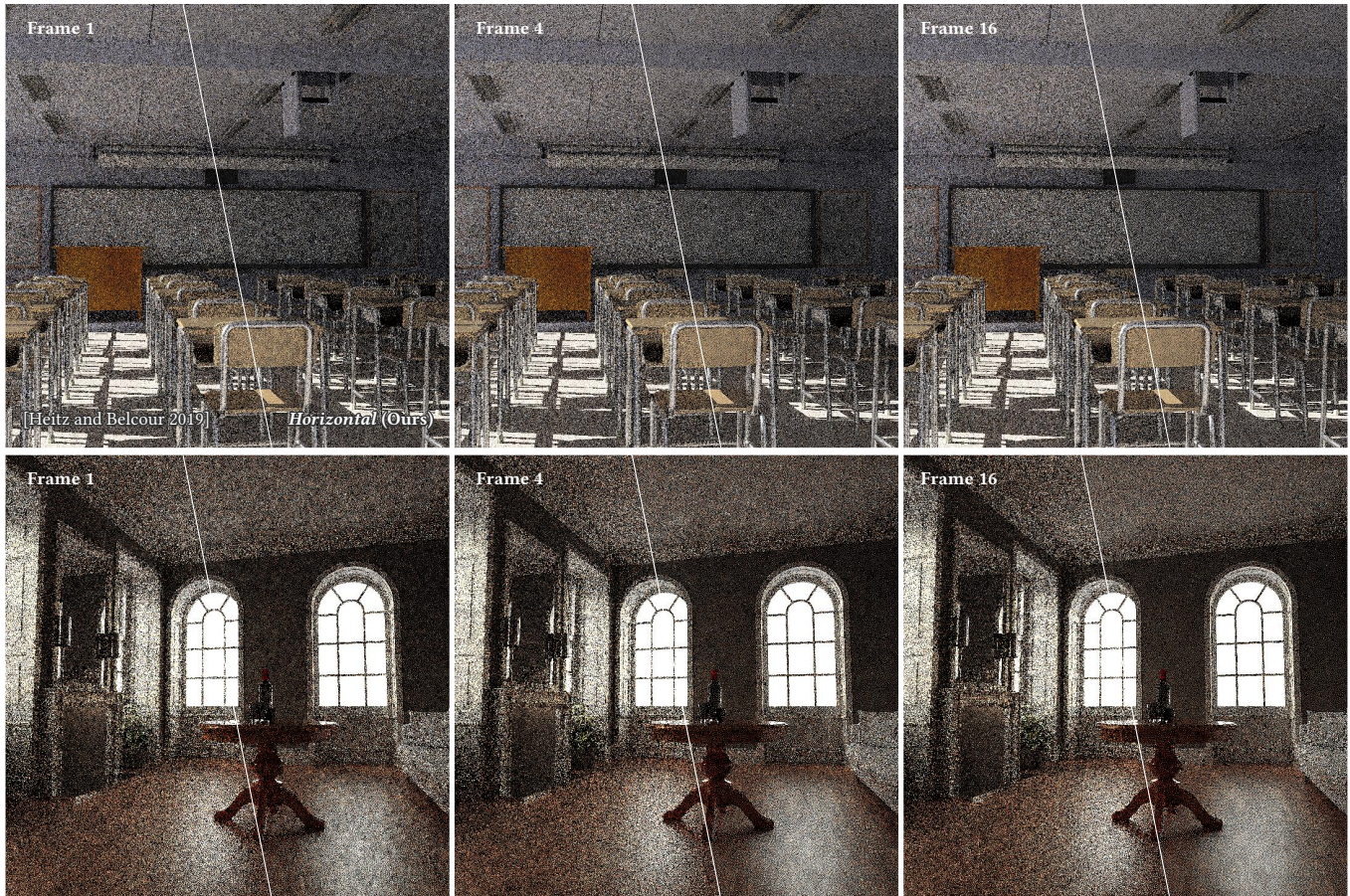


Fig. 8. Additional comparisons for horizontal approaches at 4 samples per pixel. The left side of the images are using Heitz and Belcour's permutation approach, while the right side is using our *horizontal* iterative minimization approach. The achieved blue noise distribution for our approach is consistently better.

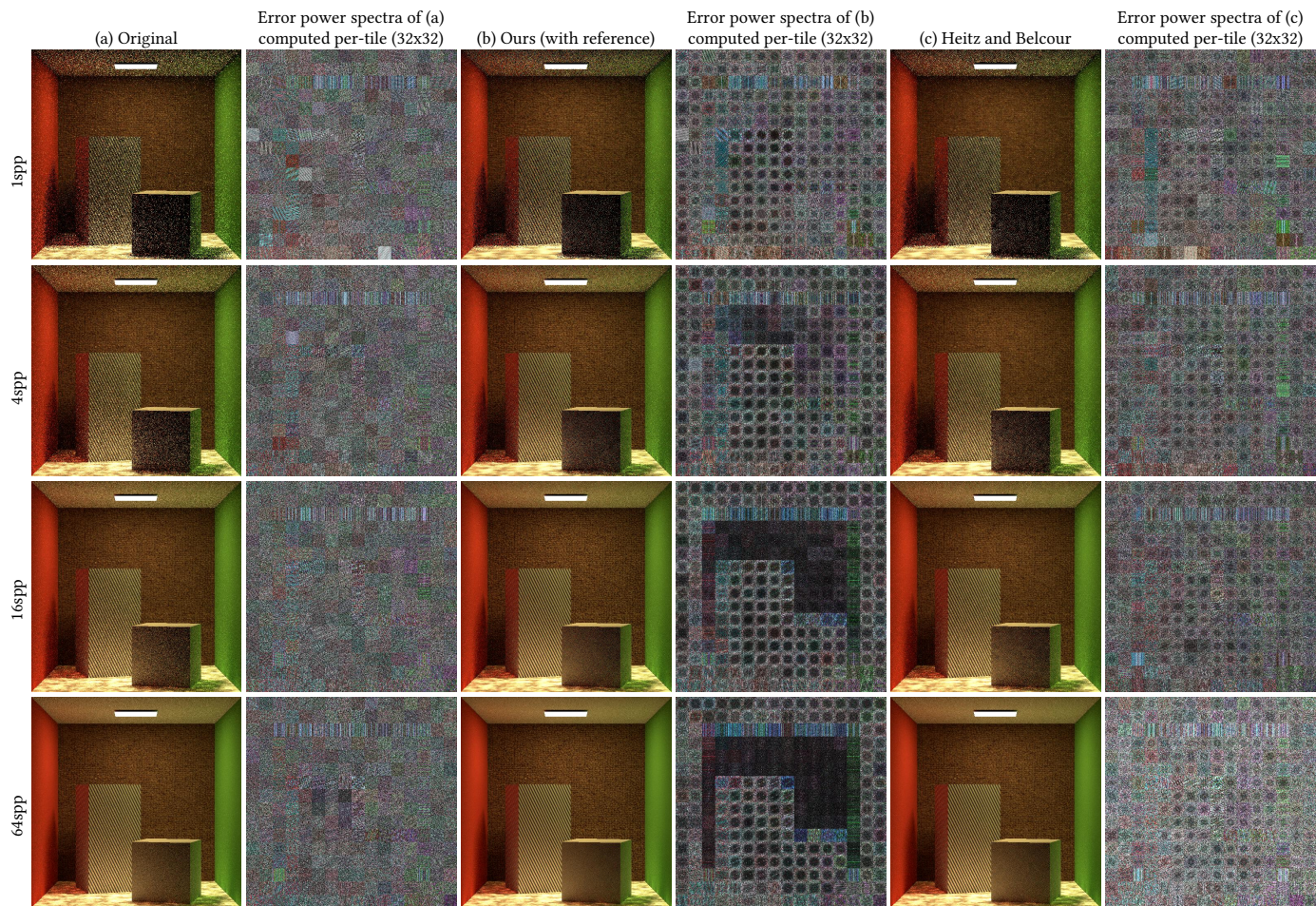


Fig. 9. The textured Cornell box scene is compared over different samples per pixel using our texture handling approach in Section 4. The improvements are visible for all spp over Heitz and Belcour’s permutation approach using demodulation. This is especially apparent when comparing the tiled error spectra. Note that the spectra are not normalized to 1.